ACS MATERIALS Au
AN OPEN ACCESS JOURNAL OF THE AMERICAN CHEMICAL SOCIETY



pubs.acs.org/materialsau
Article

# MXene-Integrated Silk Fibroin-Based Self-Assembly-Driven 3D-Printed Theragenerative Scaffolds for Remotely Photothermal Anti-Osteosarcoma Ablation and Bone Regeneration

*Published as part of the ACS Materials Au virtual special issue "2023 Rising Stars".*

Hadice Kübra Pektas, Yan. Demidov, Aslin Ahvan, Nahal Abie, Veronika S. Georgieva, Shiyi Chen, Silvia Farè, Bent Brachvogel, Sanjay Mathur, and Hajar Maleki*

Cite This: ACS Mater. Au 2023, 3, 711−726
Read Online

ACCESS | Metrics & More | Article Recommendations | Supporting Information

**ABSTRACT:** Aiming to address the bone regeneration and cancer therapy functionalities in one single material, in this study, we developed a dual-functional theragenerative three-dimensional (3D) aerogel-based composite scaffold from hybridization of photo-cross-linked silk fibroin (SF) biopolymer with MXene ($Ti_3C_2$) two-dimensional (2D) nanosheets. To fabricate the scaffold, we first develop a dual-cross-linked SF-based aerogel scaffold through 3D printing and photo-cross-linking of the self-assembly-driven methacrylate-modified SF (SF-MA) gel with controlled pore size, macroscopic geometry, and mechanical stability. In the next step, to endow a remotely controlled photothermal antiosteosarcoma ablation function to fabricated aerogel scaffold, MXene 2D nanosheets with strong near-infrared (NIR) photon absorption properties were integrated into the 3D-printed scaffolds. While 3D-printed MXene-modified dual-cross-linked SF composite scaffolds can mediate the *in vitro* growth and proliferation of preosteoblastic cell lines, they also endow a strong photothermal effect upon remote irradiation with NIR laser but also significantly stimulate bone mineral deposition on the scaffold surface. Additionally, besides the local release of the anticancer model drug, the generated heat (45−53 °C) mediated the photothermal ablation of cancer cells. The developed aerogel-based composites and chosen therapeutic techniques are thought to render a significant breakthrough in biomaterials' future clinical applications.

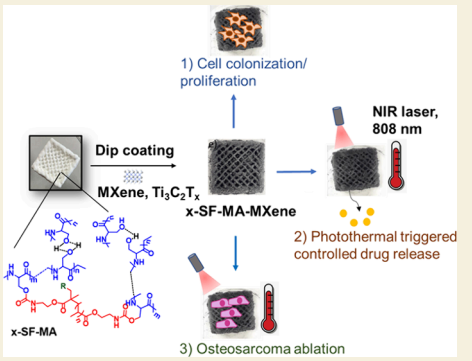


**KEYWORDS:** *aerogel, 3D scaffold, bone tissue engineering, bone cancer therapy, 3D printing, photothermal therapy, MXene*



## 1. INTRODUCTION

Every year, 2−3 million people worldwide are diagnosed with osteosarcoma, a highly malignant bone tumor. On the other hand, osteosarcoma and its treatment can cause substantial bone tissue loss and a detrimental impact on quality of life.[1] Conventional clinical strategies for addressing osteosarcoma involve a combination of surgical resection followed by subsequent radiotherapy or chemotherapy within the excised region.[2] Nevertheless, these established treatments often yield suboptimal therapeutic outcomes for patients, leading to various issues such as compromised physiological function, heightened risk of tumor recurrence and metastasis, and the occurrence of bone loss. Hence, there is a pressing need for innovative treatment modalities and the exploration of novel methodologies that can deliver improved therapeutic index and treatment efficiency.[3,4]

Currently, autologous grafts are a clinically admissible method of bone tissue reconstruction after tumor management with highly successful outcomes.[5] Despite their benefits, autograft bone is associated with some risks, such as impairment of normal body functions, limited availability, complex harvesting procedures, and donor site morbidity. Therefore, considering these limitations in both tumor therapy and bone regeneration, the development of novel approaches based on bioactive theragenerative materials (combining therapy and regeneration) for bone tumor management is of utmost importance and need.

Both cancer therapeutic potential and bone regeneration potential of developed biomaterials are governed by bio-chemical properties, such as composition, surface decorated ligands, their biophysical properties, and responsiveness to specific endogenous and exogenous stimuli. When it comes to bone tumor therapy, biomaterial-mediated tumor therapy has been mostly focused on chemo-,[6] thermo-,[7] and photo-

Received: May 16, 2023
Revised: August 20, 2023
Accepted: August 29, 2023
Published: September 8, 2023

dynamic[8] therapies. One of these techniques is biomaterial-based thermal therapy for bone tumors, recognized as a minimally invasive approach that operates by creating localized heat (at temperatures of 40−50 °C) using external triggers such as magnetic fields and light stimulation. In the realm of photothermal therapy (PTT) for bone tumors, biomaterials are commonly combined with heat-generating substances such as near-infrared (NIR) agents. These agents encompass various materials such as metals (like Au, Pt, Fe),[9,10,11] dopamine,[12,13] carbon dots,[14,15] graphene oxide,[16,17] MXene,[18,19] and black ceramics.[20] When triggered, these agents induce localized heating at the tumor site within the implantation area, ensuring that heat remains concentrated without indiscriminantly affecting healthy tissues. The application of NIR-mediated PTT (within the range of 650 to 900 nm) has been proven to achieve deep penetration into normal tissue, effectively reaching tumor sites that are otherwise inaccessible through surgical means.[21]

Bifunctional materials used recently for osteosarcoma therapy and bone regeneration include 3D-printed Fe-$CaSiO_3$ scaffold,[22] coloaded $CaO_2$ and $Fe_3O_4$ nanoparticles,[23] $SrFe_{12}O_{19}$ nanoparticle-modified mesoporous bioglass/chitosan porous scaffold,[24] and nanohydroxyapatite hybrid reduced graphene oxide (nHArGO) hydrogel,[25] to name only a few. Almost all of these bifunctional materials could kill osteosarcoma through reactive oxygen species (ROS) therapy, magnetic hyperthermia, PTT, and chemotherapy as well as combinational therapy.

Considering specific physical and microstructural characteristics such as substantial porosity, pore volume, interconnected pores, and an extensive internal surface area, aerogels prove to be exceptional biomaterials within the context of bone tissue engineering (BTE).[26] However, using bulk aerogels as a 3D biomaterial/scaffold for bone healing is also a challenging task as all aerogels (organic and inorganic) in their pristine state are mesoporous (pore size: 2−50 nm) with poor mechanical strength, which impairs their applications for *in vitro* and *in vivo* cell colonization and *in vivo* tissue ingrowth and regeneration.[27] Consequently, with the intention of tackling the existing hurdles associated with pristine ceramics and biopolymeric aerogels when utilized as optimal scaffolds in BTE, our research group has recently fabricated a range of novel synthesis and processing methodologies. In these works, we could enhance the pore size range and mechanical strength and bioactivity of aerogels through diverse surface modifications and hybridization methodologies.[26,28]

We utilized silk fibroin (SF) biopolymer as the primary building block of theragenerative aerogel scaffold of this study. We harnessed SF from the cocoons of the *Bombyx mori* silkworm as a key source of this biopolymer.[29] Its captivating properties, encompassing notable mechanical robustness, biocompatibility, biodegradability, and ease of surface modification and processing, position it as an appealing material for serving as an extracellular matrix (ECM) support for bone.[30−35] We showcased SF's inherent ability to self-assemble within the sol−gel-processable molecular precursors of tri- and tetra-functional organosilanes through the in situ method.[26,36,37] In this regard, through meticulous regulation of the sol−gel and self-assembly parameters, phase separation, and the gelation kinetics of two SF and silane phases in an aqueous solution, we developed various anisotropic functional silica[26] and silsesquioxane—[37] SF hybrid gels with an interpenetrating dual-network structure and molecular length scale homogeneity. The obtained self-assembled hybrid gels underwent additional processing through bioinspired directional freeze-casting and 3D-printing methods. This led to the creation of customized functional aerogels with enhanced mechanical strength (compressibility up to 80%), tailored macroscopic configurations, and a hierarchical pore structure encompassing micro- and nanoscale pores. These engineered aerogels demonstrated their efficacy for both *in vitro* and *in vivo* bone regeneration.[26] Our recent advancements involve the rational design of 3D-printed dual-functional aerogel scaffolds, achieved by incorporating diverse functional inorganic nano- and microparticles within the SF (bio)polymeric networks. These scaffolds have exhibited substantial potential in regulating cell−matrix interactions, augmenting osteoconductivity and osteoinductivity, and imparting antibacterial properties.[28,38]

The ease of surface modification of SF and its self-assembly capability in aqueous solution enabled us to explore further the fabrication of a range of 3D-printed functional hybrid aerogels with a controlled microstructure and macroscopic shapes. These hybrid aerogels were developed through the incorporation of various synthesized functional inorganic nano- and microparticles (carbon and ceramic), namely, hollow mesoporous silica nanoparticles,[38] graphene oxide (GO),[39] and titanium carbide nanosheets ($Ti_3C_2$, MXene),[40] into ligand-modified SF prior to self-assembly driven by robust covalent interactions, photo-cross-linking, and coordination bonds.

In this study, for the first time, we rationally designed a dual cross-linked composite aerogel scaffold through 3D printing of self-assembly-driven and photo-cross-linked SF-based aerogels coated with sorafenib-loaded MXene nanosheets. The dual-functional scaffold showed promising properties in terms of *in vitro* release of sorafenib triggered and accelerated by NIR laser irradiation of 3D-printed scaffold in acidic and neutral pH media, with potential osteoconductivity proven by *in vitro* osteoblast growth and proliferation and enhanced *in vitro* bone mineral deposition. Besides, the incorporation of MXene into the scaffold conferred additional PTT anti-osteosarcoma functionality through cell ablation thanks to the excellent NIR absorption of MXene.

## 2. METHODS

### Synthesis of Silk Fibroin Methacrylate (SF-MA)

The aqueous solution of SF was extracted from *B. mori* silk cocoons following a slightly modified protocol, as detailed by Zheng et al.[41] Initially, 5 g of silk cocoons was fragmented into small pieces and boiled for precisely 30 min in a 2 L solution of $Na_2CO_3$ (0.02 M). Subsequently, the degummed silk fibers were meticulously rinsed with ample deionized water and subsequently dried overnight at a temperature of 40 °C. Subsequently, 4 g of degummed and dry silk fibers was dissolved in 20 mL of Ajisawa's solution (comprising $CaCl_2$/EtOH/$H_2O$ in a molar ratio of 1:2:8) at an elevated temperature of 80 °C, sustained for a duration of 2 h. Following this, a solution containing 0.3 mL (equivalent to 2.13 mmol) of isocyanatoethyl methacrylate (IEMA) was introduced into the reaction vessel to achieve 15% methacrylation of the functional groups. The mixture was continuously stirred at a temperature of 60 °C for a span of 3 h. The resultant solution underwent dialysis against deionized water for 48 h, with hourly changes of water during daylight hours. After the 48 h dialysis period, the SF-MA solution was subjected to centrifugation twice, each cycle lasting 30 min at 9000 rpm. Following this, the SF-MA solution, having its concentration adjusted to 4%, was stored at a temperature of 5 °C for future use to


https://doi.org/10.1021/acsmaterialsau.3c00040
ACS Mater. Au 2023, 3, 711−726

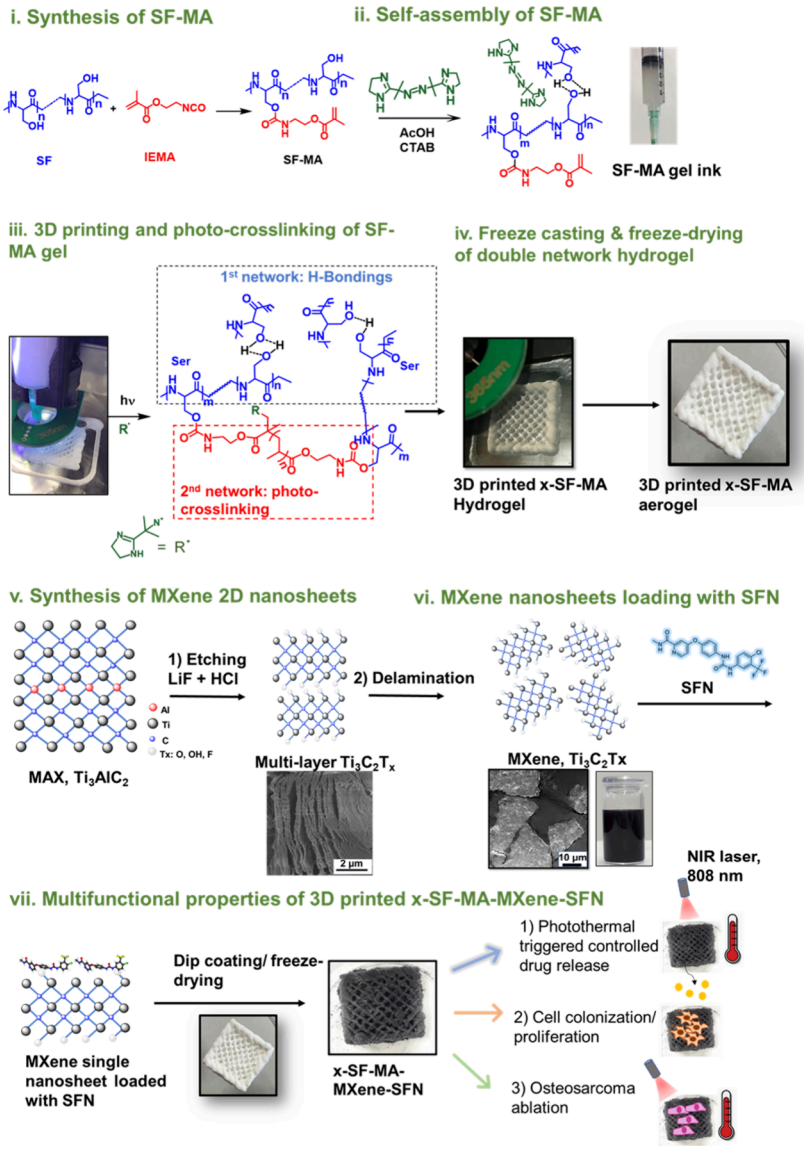


**Figure 1.** Fabrication procedure of dual-cross-linked x-SF-MA-MXene through self-assembly, photo-cross-linking-assisted 3D printing, and coating with MXene nanosheets. (i) Synthesis of SF-MA; (ii) self-assembly of SF-MA polymer into 3D-printable SF-MA gel ink; (iii) simultaneous 3D printing and photo-cross-linking of SF-MA gel ink to develop an x-SF-MA 3D scaffold; (iv) freeze-casting the x-SF-MA 3D scaffold with liquid nitrogen and freeze-drying to develop x-SF-MA aerogel scaffolds with a multiscale porous structure, pore interconnectivity, and mechanical stability; (v) synthesis of MXene 2D nanosheets from etching and delamination of the $Ti_3AlC_2$ MAX phase; (vi) MXene nanosheet loading with an SFN anticancer drug, which is followed by a coating of the 3D-printed x-SF-MA scaffold surface with resulted MXene-SFN solution and final freeze-drying of the resulted 3D scaffold; (vii) multifunctional properties of 3D-printed x-SF-MA-MXene-SFN. SEM micrographs indicate the multilayer and single nanosheets of MXene as well as the highly dispersed colloidal solution of the as-prepared MXene single nanosheet.

prevent potential storage complications arising from high concentrations.

## Synthesis of SF-MA Composite Hydrogel Inks

To synthesize the SF-MA hydrogel, the following procedure was selected. Initially, 0.5 mg of 2′-azobis-[2-(2-imidazolin-2-yl)-propane] dihydrochloride (AIPD) was introduced into a solution of acetic acid (HOAc) with a volume of 0.25 mL and a concentration of 120 mM. Subsequently, 2 mL of SF-MA (4 w/v%) was incorporated into this solution and stirred for a duration of min. The solution was then briefly preheated for 1 min on a heating plate before the addition of cetyltrimethylammonium bromide (CTAB), with a mass of 0.05 g and a molar quantity of 0.13 mmol. Following the introduction of CTAB, the solution underwent continuous stirring for min, during which the solution was intermittently heated for short periods of 1 min each. This heating was done to enhance the solubility of CTAB, ultimately resulting in the solution becoming transparent. Subsequently, the mixture was loaded into a printing syringe and allowed to undergo gelation for 1 h within an oven maintained at a temperature of 40 °C.

## 3D Printing of SF-MA Composite Gels

Thorough testing of the SF-MA composite gel was conducted to fine-tune the gelation time and gel printability. The optimal viscosity for printing was achieved at 60 min for SF-MA (containing 15% methacrylate density) at a concentration of 4 w/v%. This was carefully achieved by monitoring the gel flow to ensure continuous extrusion during printing. Subsequently, the syringe was loaded into the 3D printer, and layer-by-layer printing took place, resulting in dimensions of 20 mm × 20 mm × 5 mm according to a computer-generated 3D model. The design of this model had been previously formulated by using computer-aided design (CAD) software. The designed STL file was then translated into G codes, enabling each layer to be printed as a three-dimensional structure.


https://doi.org/10.1021/acsmaterialsau.3c00040
ACS Mater. Au 2023, 3, 711−726

During the printing process and for 10 min subsequent to printing, the gel construct was exposed to UV light with a wavelength of 365 nm. This exposure facilitated the photopolymerization of the SF-MA, leading to the creation of the photo-cross-linked 3D-printed scaffold, denoted as x-SF-MA. To enhance mechanical strength, the scaffolds underwent treatment with a mixture solution of ethanol and methanol (in a ratio of 70:30). Finally, the treated scaffolds were subjected to freeze-casting utilizing liquid nitrogen ($LN_2$) and subsequently freeze-dried at a temperature of −35 °C over a duration of 24 h.

## Synthesis of MXene, $Ti_3C_2T_x$ ($T_x$: −O, −OH, −F)

$Ti_3C_2T_x$ MXene 2D nanosheets were synthesized using the selective etching method from its bulk MAX precursor, $Ti_3AlC_2$, as described in another source.[42] A measured quantity (1 g) of lithium fluoride (LiF) powder (Alfa Aesar, >98%) was gradually introduced into 20 mL of hydrochloric acid (HCl, Thermo Fisher, technical grade, 35−38%) with a concentration of 9 M, and the mixture was stirred for a duration of 30 min. Subsequently, MAX-phase $Ti_3AlC_2$ powder (1 g) was incrementally added to this solution to initiate the etching process of the aluminum layer. This etching was carried out at a temperature of 35 °C for a span of 24 h. The resulting acidic supernatant underwent multiple rounds of centrifugation at 9000 rpm (around 8−10 times) to ultimately yield a stable, dark-green supernatant of $Ti_3C_2T_x$ with a pH of approximately 6 (as shown in Figure 1). The concentration of the $Ti_3C_2T_x$ MXene solution was determined by drying and weighing the MXene film. For simplicity, the term "MXene" will be used to refer to $Ti_3C_2T_x$ MXene throughout the rest of this study.

To prepare $Ti_3C_2T_x$ MXene suspensions for subsequent applications, the desired quantity of MXene was dispersed in ethanol (EtOH) based on the desired concentration (1 and 2 mg/mL). The resulting solution underwent ultrasonication for a duration of 1 h until a uniform suspension was achieved. Prior to ultrasonication, the suspension was flushed with argon to prevent oxidation during the ultrasonication process.

## MXene Integration into x-SF-MA Scaffolds

To prepare MXene-modified x-SF-MA scaffolds (x-SF-MA-MXene), the x-SF-MA scaffolds were first washed with boiling EtOH (for the easier removal of CTAB) for 8 h while the EtOH was changed every 2 h. The washed scaffolds were then soaked in $Ti_3C_2$ aqueous solution at different concentrations (1.0, 5.0, and 10.0 mg/mL) for 19 h at room temperature. We called the modified scaffolds as x-SF-MA-MXene-1, -5, and -10 (named as -MXene-1, -MXene-5, -MXene-10). Afterward, the MXene-modified scaffolds were washed with EtOH three times for 30 min, continued with a mixture of water/EtOH (20:80, 50:50, and 80:20) for min, and finally washed three times with deionized water each for 30 min. After washing, the modified scaffolds were freeze-cast and freeze-dried for storage to form x-SF-MA-MXene scaffolds.

## Loading of MXene Nanosheets with Sorafenib

The MXene nanosheets were loaded with the drug prior to the MXene modification of the scaffolds. The MXene powder was dispersed in the appropriate amount of EtOH, the same as the procedure above (15 mL, 1 mg/mL), and ultrasonicated for 1 h under Ar. Simultaneously, sorafenib (SFN) solution in EtOH (3 mL, 0 μg/mL) was added to the abovementioned MXene solution and was mixed and stirred at 4 °C for 2 h to allow drug loading.

## Modification of x-SF-MA Scaffolds with SFN-Loaded MXene

After washing, a blank SF-MA scaffold was cut in quarters (∼0.015 g) and each quarter of the scaffold was immersed in 2.4 mL of SFN-MXene ([SFN] 66.6 μg/mL and [MXene] 1 mg/mL) in one well of a 12-well plate. The scaffolds were left in the fridge for 19 h to allow drug loading onto the scaffold. After 19 h, the drug solution was collected, and the scaffold was gently washed with 0.5 mL of PBS.

## In Vitro Photothermal Triggered Drug Release from x-SF-MA-MXene-1-SFN-66

The drug-loaded scaffold quarters were immersed into 4 mL of acidic suspension (pH = 4.3), and PBS (pH 7) was supplemented with 1% (w/v) Tween-80 to improve the solubility of the SFN. The drug release profile was examined in two conditions with laser irradiation (808 nm, 0.80 $W{\cdot}cm^{2-}$) and without laser irradiation at 37 °C, up to 6 h (with the laser) and 7 days (without laser).

The general temperature was kept at 37 °C to simulate the body temperature during both experiments. The concentration of released SFN was monitored through UV−vis spectra at the maximum absorption wavelength of 265.5 nm.

## Photothermal Property of MXene Nanosheets and x-SF-MA-MXene-1 and -2 Scaffolds

We initially tested the photothermal-conversion properties of MXene nanosheets at different wet and dry conditions. For this, the synthesized MXene nanosheets were diluted to different concentrations (1 and 2 mg/mL) in EtOH and added to a 12-well plate (1 mL/well) with three controls for each power density and concentration. After that, the suspensions were irradiated with an NIR laser (808 nm, RLTMDL-808-1W-3, Roithner, Austria) with different power densities (0.5, 0.75, and 1.0 $W{\cdot}cm^{2-}$). The temperatures were monitored through a thermal imaging camera (Voltcraft WB-300, Germany) to evaluate the photothermal property of MXene nanosheets. Furthermore, pure and x-SF-MA-MXene-1 (5 mm × 5 mm × 5 mm) were exposed to NIR both in a dry environment (in the air) and under a wet environment (in 4 mL of PBS) with varied power densities (0.4 and 0.45 $W{\cdot}cm^{2-}$ under air, 0.4, 0.45, 0.80, and 1.0 $W{\cdot}cm^{2-}$). Finally, the photothermal stability of the MXene-modified scaffolds was tested with five laser "off−on" cycles. Scaffolds were irradiated with 0.45 $W{\cdot}cm^{2-}$ laser in dry conditions for 5 min (laser on) and then allowed to naturally cool to room temperature (laser off).

## Cell Culture and Scaffold Preparation

The MC3T3-E1 murine preosteoblast cell line was cultured in DMEM (Gibco, Thermo Fisher Scientific, USA) with an inclusion of % (v/v) fetal calf serum (FCS), 1% (v/v) penicillin (U $mL^{-1}$, Biochrom, UK), and streptomycin (0 μg/mL, Biochrom, UK) at a temperature of 37 °C and 5% $CO_2$. The identical cell culture conditions were extended to the Mg-63 cell line, as well. To ensure sterility, the scaffolds underwent UV-light sterilization for a period of 30 min, followed by sequential washing using ethanol/PBS solutions of varying concentrations (70, 50, and 30%, each for 20 min) and concluding with washing in sterile PBS (sPBS).

## Evaluation of Cell Viability

For the indirect assessment of the cytotoxicity of the scaffolds, cells were incubated with the leaching product medium. First, the sterilized scaffolds were incubated in a complete culture medium (2 mL) for 1, 3, or 5 days (three technical replicates). In addition, the culture medium was incubated for 5 days at 37 °C and served as the control medium. Next, MC3T3-E1 cells were seeded in 96 wells ($10^4$ cells/well), and after 24 h, the medium was changed to fresh medium, control medium, or medium collected from the scaffolds on day 1, 3, or 5. After 24 h of incubation, cell viability was determined by CellTiter 96 $AQ_{ueous}$ One Solution Cell Proliferation Assay (MTS). Shortly, the medium was removed and 50 μL of complete culture medium and 10 μL of reagent were added per well. After 1 h of incubation at 37 °C, absorption was measured at 492 nm (Tecan Infinite M200 PRO Reader).

## Preosteoblast Cell Attachment and Proliferation

For the direct biocompatibility and attachment assessment test, the sterilized scaffolds ( mm × mm × 5 mm) were placed in 12-well plates and seeded with MC3T3-E1 cells ($10^5$ cells per well in 1 mL of complete medium). Afterward, the cells were incubated at 37 °C, 5% $CO_2$ for 5 days, with the medium changed every second day. Biocompatibility assessment was conducted on days 1, 3, and 5. The medium was aspirated, and the cells were washed several times with


https://doi.org/10.1021/acsmaterialsau.3c00040
ACS Mater. Au 2023, 3, 711−726

sPBS followed by fixation using 1 mL of 2.5% glutaraldehyde at 37 °C for 1 h. Afterward, the fixed cells were washed with PBS and stained with 4′,6-diamidino-2-phenylindole (DAPI) for 5 min in the dark. Cell nuclei were visualized by fluorescence microscopy (Axiophot fluorescence microscope, Zeiss, Germany).

## In Vitro Photothermal Ablation of Bone Cancer Cells

To explore the potential of eradicating bone cancer cells (specifically the MG63 cell line), the cell viability of cells seeded on two distinct scaffold formulations (x-SF-MA and x-SF-MA-MXene-1) was assessed under NIR laser irradiation at three different time intervals: 1, 3, and 7 days. The scaffold samples were fashioned into cubic shapes (6.5 mm × 6.5 mm × 5 mm) and situated within 24-well cell culture plates. For each scaffold variant, $10^4$ MG63 cells were seeded per well in 1 mL of DMEM medium. Three samples from each formulation underwent cell seeding, and an additional sample was designated as a control, devoid of any cell seeding.

To investigate the possibility of eliminating cancer cells through near-IR laser exposure, the samples were subjected to laser irradiation at each time point. The laser beam utilized had a wavelength of 808 nm, with a power density of 0.85 W/m$^2$, administered for durations of 5 and 20 min. The temperature changes within the scaffolds were monitored through a photothermal camera, and the cell viability on the irradiated scaffolds was evaluated by employing the AlamarBlue assay.

To carry this out, 1 mL of a 10% AlamarBlue solution was introduced to each scaffold and incubation was allowed for a period of 4 h. Following the incubation duration, 100 $\mu$L of the solution from each sample was transferred to a 96-multiwell plate in triplicate (3 × 0 $\mu$L from each sample). Subsequently, the cell metabolism was measured by using a fluorescence spectrophotometer (Tecan GENios) with excitation at 540 nm and emission at 595 nm. The measurements were recorded in relative fluorescence units (RFU), and the formula used for the analysis was

$$\mathrm{RFU_{total}} - \mathrm{RFU_{Control}} = \mathrm{RFU_{seededcells}} \tag{1}$$

Following each NIR irradiation session, the seeded scaffold underwent a live/dead assay utilizing Calcein AM for live cell staining and propidium iodide (PI) for staining dead cells. Following an incubation period of 45 min, the staining solution was removed and the samples were washed with Dulbecco's phosphate-buffered saline (DPBS) before being subjected to analysis via fluorescent microscopy (Olympus BX51WWI) at a magnification of 40×. The live cells were identified by their green staining, with an excitation wavelength of 490 nm and an emission wavelength of 515 nm, derived from Calcein/AM. In contrast, the dead cells were distinguished by their red staining, featuring an excitation wavelength of 535 nm and an emission wavelength of 617 nm due to PI.

## Biodegradation of x-SF-MA-MXene-1 Scaffolds

The x-SF-MA-MXene aerogel-based scaffolds, measuring 2 cm × 2 cm × 0.5 cm, were sectioned into quarters, and the initial weight ($W_0$) of each individual sample was documented. Subsequently, the samples were positioned within a 12-well plate and immersed in respective degradation media: phosphate-buffered saline (PBS) and proteinase K (PK) solution (0.5 U/mL). This incubation occurred at a temperature of 37 °C in a shaking water bath, extending for a duration of up to 21 days. To maintain the degradation process, the degradation media were replaced every 2 days, with the used media stored at 4 °C and fresh degradation media added to the samples in the plate each time.

At specific intervals (7, 14, and 21 days), the samples that remained were taken out of the liquid environment and their weight ($W_t$) was measured following freeze-drying at a temperature of −40 °C for 24 h.

The weight reduction of the samples was represented as $W_d = (W_0 - W_t)$, encompassing losses from two distinct constituents: an inorganic component (MXene and $Ti_3C_2$) and an organic component (SF-MA-30). The extent of degradation was evaluated by expressing the percentage weight loss as

$$\text{total deg. of scaffold}(\%) = \frac{W_d}{W_0} \times 100\%,\ W_d = W_0 - W_t \tag{2}$$

The weight loss attributed to the inorganic components ($W_i$) could be ascertained by analyzing the concentration of Ti(III) within the collected degradation media using a spectrophotometric assay. Given the absence of a direct method for quantifying released Ti(III) ions stemming from MXene degradation, the Ti(III) present in the degraded solution (supernatant) was initially converted to Ti(IV). This conversion was achieved by oxidizing Ti(III) to Ti(IV). As per eq 3, under acidic conditions, Ti(IV) ions undergo a reaction with hydrogen peroxide, resulting in the formation of a yellow-orange complex denoted as $[TiO{\cdot}H_20_2]^{2+}$. This complex formation serves as the foundation for the widely recognized technique used to quantify the titanium content.

$$\mathrm{Ti(III) + H_2O_2 \rightarrow Ti(IV) + OH^- + OH\cdot} \tag{3}$$

To establish a calibration curve for Ti(IV), we initially dissolved 0.6903 g of Ti-*n*-butoxide in a mixture of 5 mL of $HNO_3$ and $H_2O$ (1:1). This solution was further diluted to 0 mL in a volumetric flask, resulting in a 1 mg/mL standard titanium solution. Subsequently, we transferred varying volumes (0.0, 0.65, 1.3, 1.96, and 2.6 mL) of the 1 mg/mL standard titanium solution to separate the 25 mL volumetric flasks. To each flask, we added 0.5 mL of $H_2SO_4$ and 1 mL of 30% $H_2O_2$. Following a 10 min interval, we gauged the absorbance of the solutions within a wavelength range of 300−500 nm against water using UV−vis spectrophotometry, with the maximum absorbance ($\lambda_{max}$) detected at 4 nm. This procedure was conducted to establish a calibration curve for Ti(IV). For the measurement of Ti(III) in the sample degradation supernatant collected in a certain period, 1 mL of each media solution was added with 0.5 mL of $H_2SO_4$ and 1 mL of 30% $H_2O_2$. Since the Ti(III) concentration is too low, here, we do not dilute it to 25 mL. After 10 min, we measured the absorbance of the solution ranging from 300 to 500 nm vs water by UV−vis spectrophotometry with $\lambda_{max}$ = 4 nm.

The weight loss attributed to the inorganic fraction ($W_i$) was determined by using the calibration curve of Ti(IV). Subsequent to this, the weight loss arising from the degradation of the organic fraction ($W_{SF}$) was determined by $W_d - W_i$. Consequently, the degradation of SF can be computed as follows:

$$\text{inorganic fraction (MXene) deg. } (\%) = \frac{W_i}{W_0} \times 100\% \tag{4}$$

$$\text{organic fraction (SF)deg. } (\%) = \frac{W_{SF}}{W_0} \times 100\%,\ W_{SF} = W_d - W_i \tag{5}$$

## Biomineralization Assay

*In vitro*, the process of acellular biomineralization on the scaffold's pore surface was investigated by subjecting the scaffolds to incubation with a simulated body fluid (SBF) solution. The SBF solution was formulated based on the methods developed by Kokubo and Takadama.[43] This solution was designed to replicate the ion types and concentrations present in human plasma. The sterilized x-SF-MA and x-SF-MA-MXene-1 aerogel matrices were subjected to incubation in SBF at distinct time intervals of 1, 3, 7, and 14 days, all maintained at a temperature of 37 °C. Each day, fresh SBF was introduced to replace the previously incubated solution. At the culmination of the incubation period, the matrices underwent freeze-drying.

The formation and morphology of hydroxyapatite crystals within the scaffolds were assessed using field emission scanning electron microscopy (SEM) and X-ray diffraction analysis, employing Mo K$\alpha$ radiation.



https://doi.org/10.1021/acsmaterialsau.3c00040
ACS Mater. Au 2023, 3, 711−726

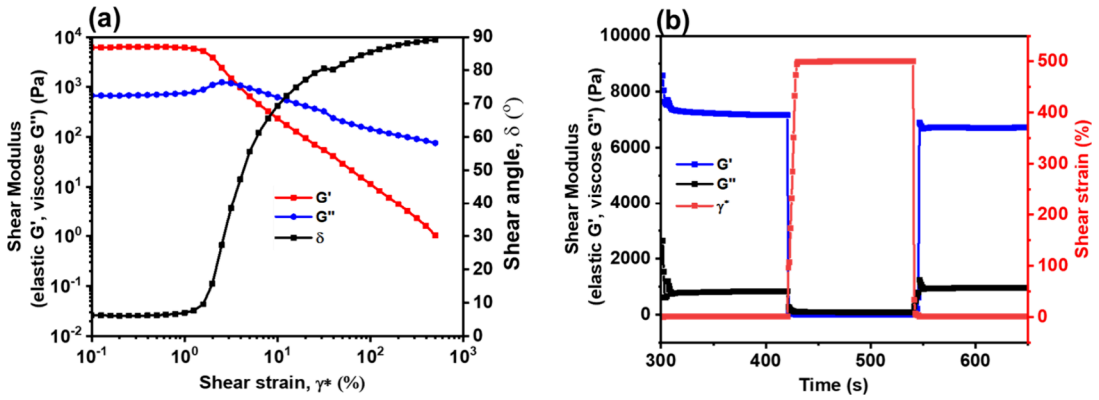


**Figure 2.** (a) Amplitude sweeps of the SF-MA gel with elastic shear modulus $G'$ (red curve), viscous shear modulus $G''$ (blue curve), and phase angle ° (black curves) as a function of the complex shear deformation $\gamma^*$. (b) Three-phase jump test of the SF-MA gel sample with elastic shear modulus $G'$ (blue curve), viscous shear modulus $G''$ (black curve), and shear deformation $\gamma^*$ (red curve) as a function of time.

## 3. RESULTS AND DISCUSSION

### Self-Assembly, Photo-Cross-Linking-Assisted 3D Printing, and MXene Coating Processes

We began the synthesis of aerogel scaffold by first creating SF methacrylate (SF-MA) as the primary constituent, which possessed the unique properties of self-assembly and photo-cross-linking. This involved modifying the −OH, $-NH_2$, and −COOH functional groups on SF macromers by incorporating the isocyanate groups of IEMA through urethane, urea, and amide bonds. This introduced vinyl bonds of IEMA to the SF-MA macromers. Figure 1i demonstrates the formation of urethane in SF macromers through the reaction of surface −OH groups with IEMA, primarily due to the abundant −OH groups present in the SF chains.

Next, we subjected the SF-MA solution to a one-step self-assembly process at pH 4, in the presence of the cationic surfactant CTAB. This resulted in the formation of a homogeneous gel in just about an hour. It was observed that compared to SF-MA alone, which required several days for self-assembly and gelation at higher concentrations, a catalytic amount of CTAB surfactant accelerated the gel formation by facilitating the SF-MA self-assembly. CTAB's amphiphilic nature allowed it to envelop the hydrophobic parts of SF-MA, reducing the surface tension of SF solutions, forming hydrogen bonds with SF-MA, and ultimately leading to the creation of SF-MA hydrogels.[38]

To achieve a seamless flow during gel extrusion, the viscosity of the gel was meticulously fine-tuned by controlling the gelation time. In a previous study, we successfully optimized the printing parameters of the SF gel by experimenting with different concentrations and gelation times of SF-MA.[38] A continuous gel flow, rendering the material printable and shapeable, was achieved within 60−70 min after initiating the gelation of SF-MA (4%) with 15% methylation density. Notably, the gel printability remained unaffected by the degree of methacrylation. However, the initial concentration of SF-MA played a critical role in determining both the gelation time and its printability.[38]

Rheological properties of gel (NETZSCH Kinexus ultra+ rotational rheometer) were studied to evaluate the gel mechanical strength and shear thinning (deformability and recovery behavior) upon applied shear stresses, e.g., extrusion through a nozzle. The gel's shear thinning is a crucial characteristic that validates the gel's printability, as it influences the gel flowability under shear stress applied in the printing nozzle. Additionally, it determines the material's ability to recover its shape after being released from the nozzle and when the shear stresses are removed.[44]

Figure 2a shows the amplitude sweep for the SF-MA gel as a function of complex shear strain or shear deformation. The amplitude sweep provides values for the strength/stability of a given material/sample. At the beginning of the measurement, the value for the elastic shear modulus $G'$ was ca. 6039 Pa and for the viscous shear modulus $G''$ it was ca. 696 Pa. Between a shear deformation of 0.1% and 1.3%, the linear viscoelastic region of the specimen could be observed. However, with increasing deformation, the elastic and viscous moduli showed a decreasing behavior and, thus, a departure from the gel's linear viscoelastic region (LVER). The phase angle increased up to almost 90° at 500% deformation.

We further evaluated the gel self-healing and shear-thinning performance using the three-phase jump test (Figure 2b). At the beginning of this measurement, in the first phase, the gel was subjected to a complex shear deformation of 1% for a duration of 2 min. Subsequently, in the second phase, a deformation of 500% was applied for 2 min with a rapid drop in gel for both shear moduli's values (storage and loss). Finally, in the third phase, another 1% shear deformation was specified to determine the gel's structure recovery or structure buildup as a function of time. Here, the SF-MA gel showed an immediate increase in both shear moduli at the end of the second phase and at the beginning of the third phase, respectively, confirming the gel's appropriate rheological behavior upon printing by microextrusion-based 3D printing.

The SF-MA gel, once developed, was printed directly from the CAD model. During the printing process, the methacrylate functionals on SF chains underwent photo-cross-linking simultaneously with the gel extrusion.

The creation of robust 3D scaffold structures characterized by hierarchical porosity was accomplished by synergistically integrating self-assembly and photo-cross-linking techniques. In the subsequent stage, to establish additional interconnected porosities essential for cellular communication between the printed struts and pore walls, the fabricated scaffolds underwent unidirectional freeze-casting.[45−47] By inducing one directional growth of ice crystals within the gels followed by their subsequent elimination via sublimation, a new set of interconnected porosities was created. These porosities acted as negative replicas of the ice crystals grown within the gel. As


https://doi.org/10.1021/acsmaterialsau.3c00040
ACS Mater. Au 2023, 3, 711−726

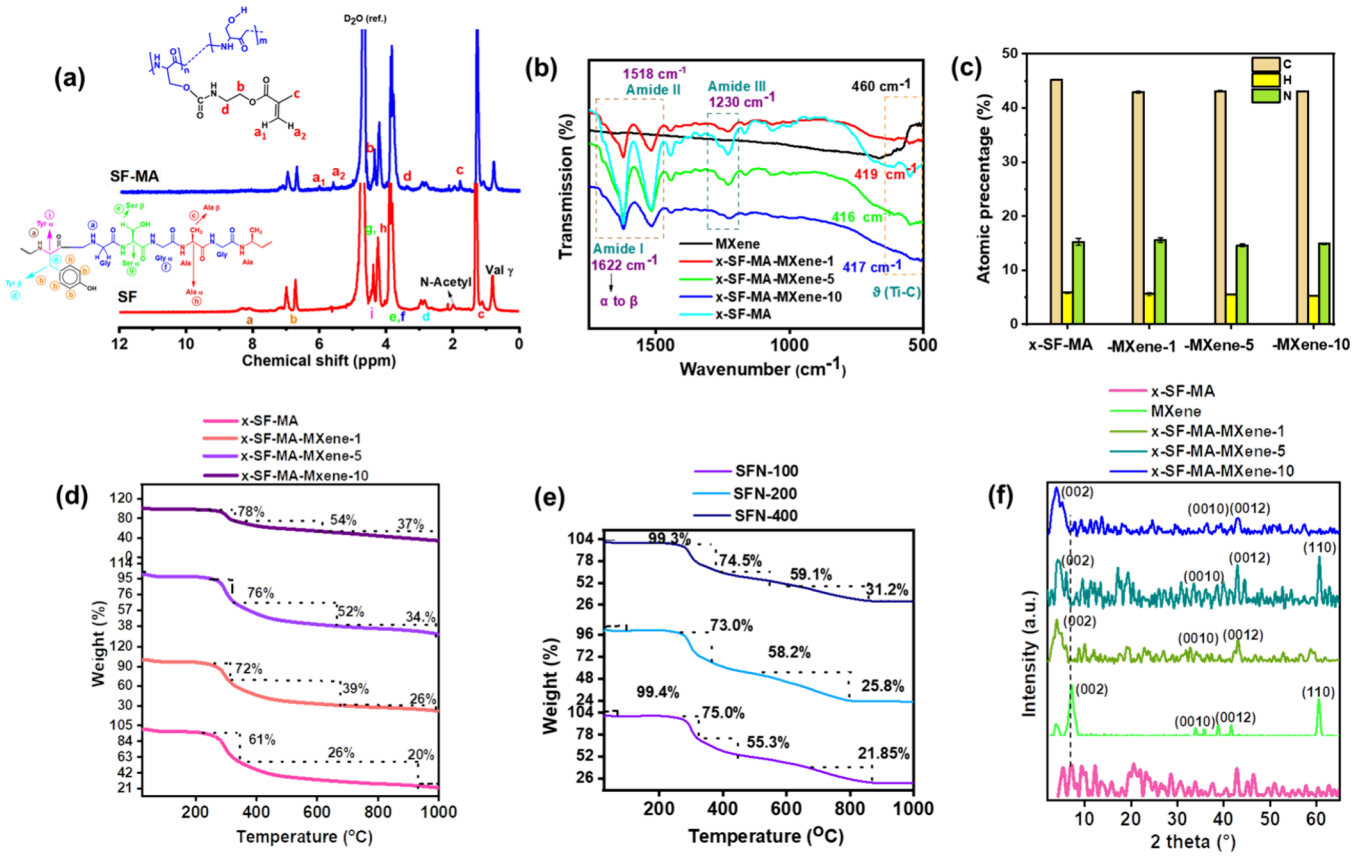


**Figure 3.** (a) $^{1}$H NMR spectra of SF and SF-MA. (b) ATR-FTIR spectra. (c) CHN elemental analysis. (d) TGA of x-SF-MA and x-SF-MA-MXene-1, -5, and -10. (e) TGA of SFN-loaded composite scaffolds at different concentrations. (f) XRD patterns of MXene and x-SF-MA and x-SF-MA-MXene-1, -5, and -10. SFN-0, 200, and 400 are the abbreviated forms of x-SF-MA-MXene-1-SFN-0, -200, and -400 composite aerogels.

previously shown, these micron-sized freeze-cast pores (approximately 20 $\mu$m) were limited in size and only capable of accommodating osteoblast cells on the gel network surface.[26] Furthermore, the potential for osteoblasts to penetrate deeply into bulk freeze-cast gels remains limited. In very recent studies,[28,38] our group has demonstrated that 3D printing of scaffolds offers the opportunity to engineer large porosities (ranging from 500 to 00 $\mu$m) within the aerogel matrix. This enables osteoblast infiltration inside the gel network through the creation of hierarchically interconnected porosities.

In the next step, to endow photothermal properties to the 3D-printed x-SF-MA construct, we modified the 3D-printed scaffold surface with MXene 2D ceramic nanosheets through a simple dip coating process (cf. Figure 1).

MXenes (here $Ti_3C_2T_x$, $T_x$ denotes −O, −F, and −OH functional groups) are newly emerged (2D) nanosheets of transitional metal carbides that are prepared by etching the Al layer in the bulk MAX, $Ti_3AlC_2$ phase[48,49] (cf. Figure 1v). The unique composition and surface chemistry of MXenes make them intriguing for many fascinating properties, such as their superior hydrophilicity, the coexistence of metallic and semiconductor electronic conductivity, and broad optical absorption.[42,50] As a result of these properties, in the last 5 years, MXenes have been extensively studied for applications including cancer treatment, bioimaging, biosensors, and antibacterial agents.[51−53] The substantial absorption of NIR light by MXenes facilitates effective PTT within the NIR-I/II biowindows.[54,55,56]

In this work, in order to imbue the scaffold with capabilities for chemotherapy and PTT, we introduced modifications to the surface of 3D-printed x-SF-MA aerogel scaffolds. This was achieved through the incorporation of SFN-loaded MXene. Subsequently, the modified scaffolds underwent freeze-casting and freeze-drying procedures, resulting in the creation of composite scaffolds termed the x-SF-MA-MXene-SFN aerogel (as illustrated in Figure 1vi). The fabricated composite scaffolds are hypothesized to have multiplex functionalities of (1) photothermally triggered controlled drug release enabling on-demand drug release in cancer-resected implanted sites, (2) high cell colonization necessary for implant osteoconductivity and bone ingrowth requirement, and (3) the photothermal eradication of bone cancer cells, which was executed by subjecting the scaffold to NIR laser irradiation before studying the colonization of preosteoblasts (as depicted in Figure 1 vii). All of these challenges are followed in this study.

## Chemical, Crystalline, and Microstructural Properties

The SF methacrylation process was confirmed by using $^{1}$HNMR spectroscopy. Figure 3a showcases the $^{1}$H resonances of SF, which encompass a combination of resonances arising from random coils, loops, and strands.[57,58] The blue spectrum in this Figure is representing SF-MA, which exhibits the identical peaks as the SF spectrum, alongside extra peaks corresponding to the methacrylate groups of SF.[30] Particularly, the doublet peaks at 6.37 and 6.5 ppm can be attributed to the $a_1$ and $a_2$ vinylic protons of the methacrylate functional groups, respectively. Additionally, the peak at 1.8 ppm corresponds to the methyl group (identified as peak c) while the peaks at 3.8


https://doi.org/10.1021/acsmaterialsau.3c00040
ACS Mater. Au 2023, 3, 711−726

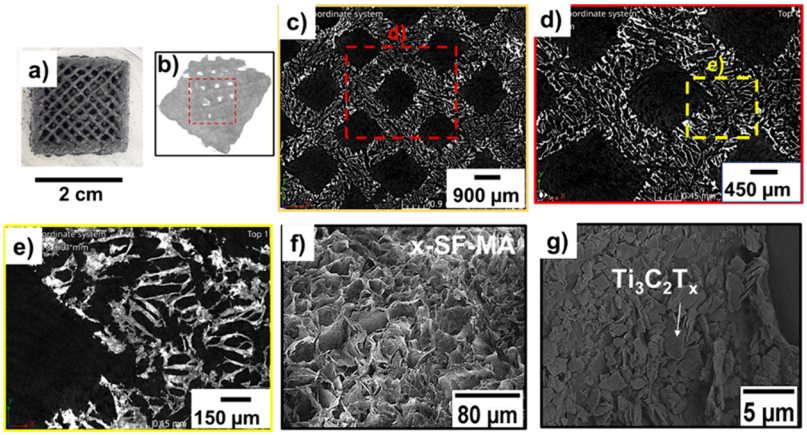


**Figure 4.** (a) The x-SF-MA-MXene-1 3D-printed aerogel structure measuring 2 cm in lateral size with a 1 mm grid size. (b–d) Microcomputed X-ray tomography at various levels of magnification. (e) Nanocomputed X-ray tomography revealing porous structures' details within the same sample. (f, g) Scanning electron microscopy (SEM) micrographs illustrating x-SF-MA (10×) and x-SF-MA-MXene-1 (15×), respectively.

and 4.4 ppm are linked to the $CH_2$– protons of d and b, respectively.

The ATR-FTIR spectra at Figure 3b show the characteristic amide bonds of SF, namely, amide I ($\vartheta_{as}$ (C═O) at 1638 $cm^{-1}$), amide II (($\delta_s$ (N–H) deformation/bending at 1514 $cm^{-1}$), and amide III $\vartheta_{as}$ (C–N) at 1230 $cm^{-1}$) for x-SF-MA. The x-SF-MA composite scaffolds modified with different MXene concentrations (1, 5, and mg/mL) exhibit all the characteristic amide bands of SF: amide I at 1622 $cm^{-1}$, amide II at 1518 $cm^{-1}$, and amide III at 1230 $cm^{-1}$, where the amide I band also has the high intensity and is shifted to higher wavenumbers in comparison to the amide I band of the SF polymer. This is explained by conformational changes from the $\alpha$-helix to the $\beta$ sheet in x-SF-MA aerogels.[59] The spectrum for MXene shows a characteristic band at 460 $cm^{-1}$ belonging to the Ti–C stretching.[60] This vibration is shifted to 416 and 419 $cm^{-1}$ for the aerogel composites, demonstrating the successful interaction of MXene with the x-SF-MA surface.

CHNS elemental analysis in Figure 3c for x-SF-MA and x-SF-MA-MXene-1, -5, and -10 indicates a decreasing trend in the elemental percentage of C, H, and N with an increasing amount of MXene in the composite. The decreases in C, H, and N element percentages are due to the contribution of the heavy Ti element of MXene nanosheets and the surface –F groups, originating from $T_x$ surface terminal groups.

The thermal stability evaluation with thermogravimetric analysis (TGA) in Figure 3d indicates the decomposition of x-SF-MA at ∼260 °C, which is associated with the cleavage of the peptide bonds on the polyamide chains of SF. Incorporating MXene into the scaffolds shifts the decomposition temperature to ∼270 °C, increasing up to ∼280 °C with a higher amount of MXene. While the rest mass of x-SF-MA is 20.8%, the introduction of MXene into the x-SF-MA aerogel results in a higher overall rest mass: MXene-1:27%, MXene-5:34%, and MXene-10:37%, which are according to the MXene theoretical values in aerogel composites: MXene-1:25.6%, MXene-5:32.20%, and MXene-10:36.2%. The loading of the SFN to the scaffold results in an overall decrease in thermal stability, as seen in Figure 3e. However, a higher SFN concentration enhances stability. This increase in stability is caused by the aromatic rings in SFN. In general, the increase and decrease in the thermal stability of the scaffolds can be explained by the hydrocarbon ratio, ceramics, and aromatic rings.

Powder X-ray diffraction (XRD) patterns in Figure 3f exhibit characteristic peaks at 2$\theta$ values *of* 12.3, 19.8, 23.3, and 28.7° for x-SF-MA, which are assigned to the silk I (random coil) crystal structure in SF. The peaks at 9.5 and 20.6–20.9° are attributed to the silk II crystalline structure ($\beta$ sheet).[61] For pristine MXene, the most intense peak at 7.2° (002) is attributed to the MXene basal plane upon selective etching of Al layers from $Ti_3AlC_2$ (MAX) precursors, which introduces the surface terminal groups of –OH, –F, and –Cl.[42] This peak also indicates the interlayer distance or the *d* spacing of MXene.

Coating of x-SF-MA aerogel scaffolds with MXene nanosheets caused a shift in 2$\theta$ values for (002) characteristic peaks from 7.1 to 5.9, 6, and 5.1° for -MXene-1,- 5, and -10, respectively. This is explained by less order in the *c* direction upon dispersion of the nanosheets in the aerogel and increasing the *d*-spacing from 0.85 to 1.01 1.02, and 1.20 nm, respectively, based on the Bragg equation: $2d\sin\theta = n\lambda$. Therefore, the presence of the diffraction peaks of MXene in x-SF-MA-$Ti_3C_2$Tx scaffolds confirms the successful incorporation of MXene.

Figure 4a depicts the optical image of the 3D-printed x-SF-MA-MXene-1 scaffold featuring a lateral dimension of 2 cm. Through a combination of X-ray micro- and nanocomputed tomography techniques in Figure 4b–e and SEM micrographs in Figure 4f, the internal microstructural patterns are seen from a multiscale standpoint and the 3D scaffold is found to be hierarchically porous. At a smaller length scale, the scaffold exhibited a micromorphology resembling a honeycomb structure, characterized by pores ranging between 0 and 120 $\mu$m. These pores were a result of the amalgamation of self-assembly, photo-cross-linking, and entanglement of x-SF-MA macromers, combined with the growth of ice replicas during the freeze-casting process. This enabled the interconnection of larger pores (developed by the 3D printer, measuring 00 $\mu$m) within the scaffold. Consequently, the pore size range achieved through the combination of 3D printing and freeze-casting falls within the spectrum of bone pore sizes, specifically between 0 and 00 $\mu$m. This range is critical for facilitating cell proliferation, vascularization, and ensuring adequate mechanical strength, as required in BTE.[62] Figure 4g indicates MXene nanosheet integration on the pore surface of x-SF-MA scaffolds while keeping their single-sheet morphology without agglomeration during the coating.


https://doi.org/10.1021/acsmaterialsau.3c00040
ACS Mater. Au 2023, 3, 711–726

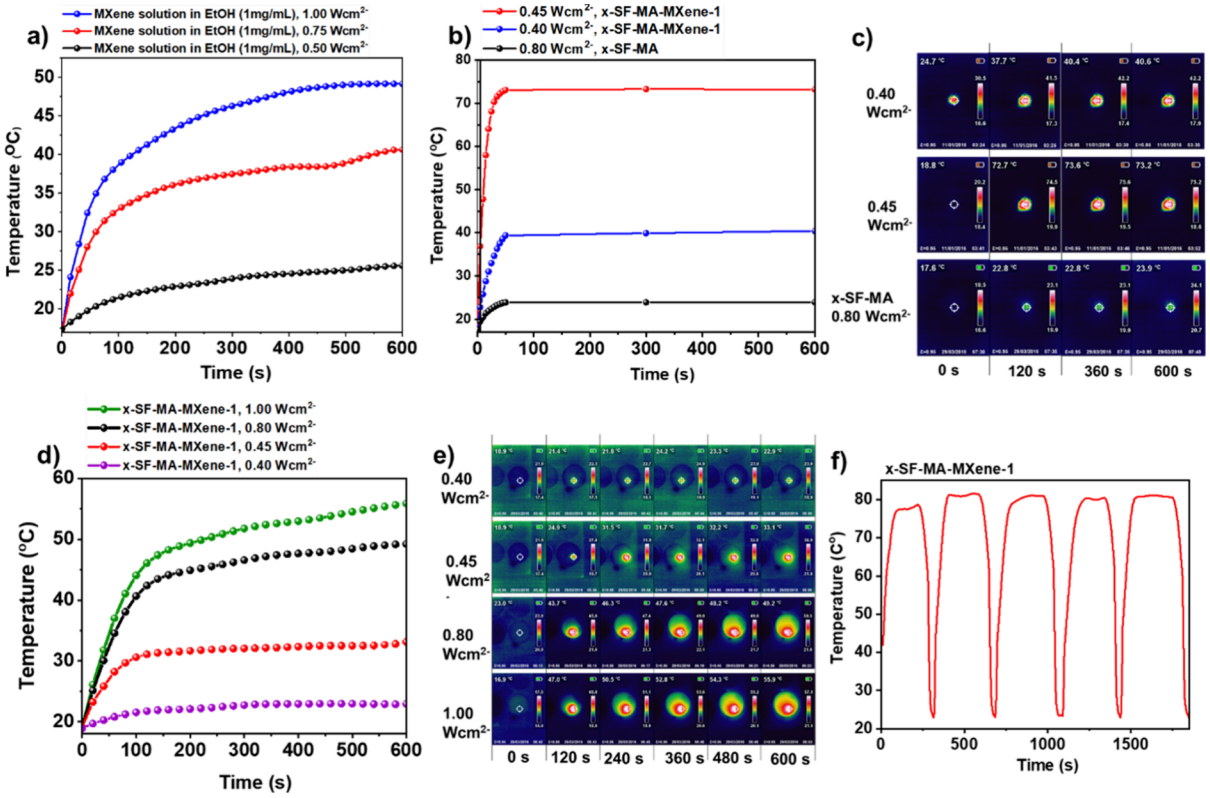


**Figure 5.** (a) Evaluation of the photothermal efficacy of MXene (1 mg/mL in EtOH) through 808 nm laser irradiation at varying power densities. (b) Assessment of the photothermal effectiveness of x-SF-MA and x-SF-MA-MXene-1 scaffolds under 808 nm laser exposure at different power densities within a dry environment. (c) Utilization of images of thermal camera illustrating the temperature distribution in scaffolds with and without MXene modifications and subjected to various power densities over a span of 10 min. (d) Examination of the photothermal capability of x-SF-MA-MXene-1 scaffolds under 808 nm laser irradiation with diverse power densities while immersed in a 4 mL PBS solution. (e) Employment of thermal camera images displaying the registered temperature fluctuations in x-SF-MA-MXene scaffolds when subjected to distinct power densities within a 10 min interval. (f) Investigation into the photothermal robustness of x-SF-MA-MXene-1 scaffolds in a dry environment utilizing a power density of 0.45 W $cm^{-2}$. The scaffolds underwent a cyclic process where they were irradiated with the laser for 5 min (laser on) and subsequently left to naturally cool down to room temperature (laser off), a process lasting approximately 30 s. This cycle was repeated five times.

## Photothermal Property of MXene and x-SF-MA-MXene-1 and Photothermal Triggered Cumulative Release of SFN

PTT has shown great potential as a noninvasive cancer treatment approach through hyperthermia or thermal ablation of malignant cells. The ideal photothermal nanoagents for photonic tumor hyperthermia treatment should have high optical absorption as well as high photothermal-conversion efficiency in the NIR biowindow.[63] Functioning as an innovative photothermal agent, $Ti_3C_2$ MXene[18] can effectively eliminate cancer cells by transforming the light energy from laser irradiation into heat energy. This process offers precise spatiotemporal control within the NIR-I/II biowindow (wavelength, $\lambda$ = 626−1316 nm).

In this study, integration of MXene into the x-SF-MA 3D-printed scaffold surface introduced significant photothermal effects to overall composites through irradiation with NIR photon (808 nm). To assess this, we initially studied the photothermal activity of MXene colloidal solution alone at constant concentrations (1 mg/mL) and various laser power densities (PDs, the intensity of incident light: 0.5, 0.75, and 1.0 W $cm^{-2}$). As seen from Figure 5a, MXene nanosheets possess a high photothermal-conversion efficiency correlated with the PD of the laser photon. The higher the PD, the higher the heat generated with nanosheets. For example, at PD = 1.0 W $cm^{-2}$, 10 min after starting the illumination in the solution, the generated heat on the scaffold surface reached the highest values (47 °C) and became constant.

We have also assessed the photothermal properties of the x-SF-MA-MXene-1 composite scaffolds in both dry (under air) and wet conditions (in PBS), shown in Figure 5b−e. According to the thermal camera images shown in Figure 5c, the temperature rises on the x-SF-MA-MXene-1 scaffold have occurred rapidly in a dry environment and reached 40 and 70 °C in 1 min with a PD of 0.4 and 0.45 W·$cm^{-2}$, respectively. The temperature difference between dry and wet conditions is attributed to the heat dissipation in the liquid during the photothermal-conversion tests. While MXene-modified aerogel composites readily reached the desired temperature for cancer cell ablation (45−50 °C) (cf. Figure 5e), the x-SF-MA scaffolds exhibited no temperature changes even after min of laser irradiation. Based on these results, the fabricated x-SF-MA-MXene-1 is suitable for anti-osteosarcoma implanting materials for remotely treating bone tumor at the implant site.

The photothermal durability of the x-SF-MA-MXene-1 scaffolds was additionally explored in a dry environment using a laser PD of 0.45 W·$cm^{-2}$. To conduct this test, the scaffolds were subjected to laser irradiation for a duration of 5 min (laser on) and subsequently permitted to return to room temperature (laser off) within a span of 30 s. As shown in Figure 5f, x-SF-MA-MXene-1 scaffolds have shown excellent photothermal stability within five repetitive irradiations under


https://doi.org/10.1021/acsmaterialsau.3c00040
ACS Mater. Au 2023, 3, 711−726

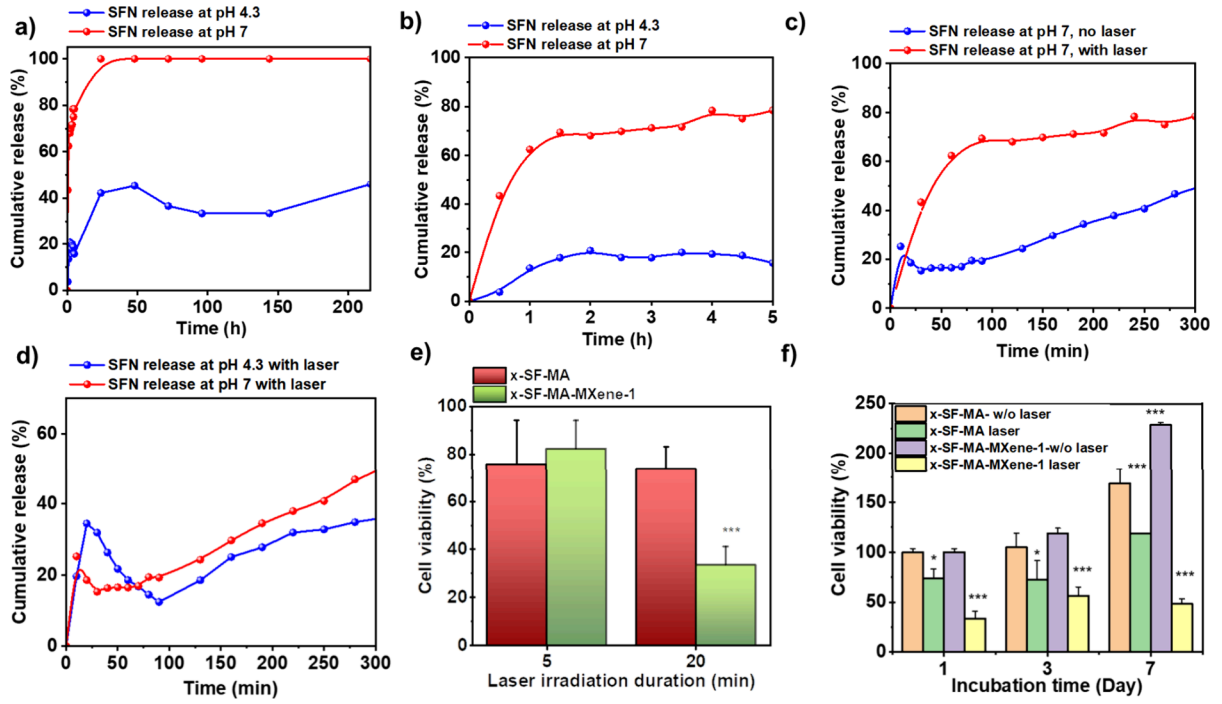


**Figure 6.** Cumulative SFN drug release profiles from 3D-printed x-SF-MA-MXene-1-SFN-0 scaffolds were evaluated across varying pH levels, encompassing both laser irradiation and nonirradiation conditions. (a) Monitoring the SFN release from the scaffolds within acidic and neutral pH environments at 37 °C over a span of 9 days without laser irradiation. (b) Investigation into the initial SFN release from the scaffolds under acidic and neutral pH conditions at 37 °C within the first 5 h, also excluding laser irradiation. (c) Tracking the SFN release from the scaffolds within a neutral pH environment, under both laser irradiation and nonirradiation conditions, during a 5 h time frame. (d) Examination of SFN release from the scaffolds under both laser irradiation and nonirradiation conditions under the influence of laser irradiation, over a 5 h interval. (e) Study of the impact of varying laser irradiation durations (5 and 20 min) with a power density of 0.85 W $cm^{-2}$ on the viability of bone cancer cells and hyperthermia, in a setup involving seeding on x-SF-MA-MXene-1. (f) Calculation of the relative cell viability of bone cancer cells planted on x-SF-MA and x-SF-MA-MXene-1 scaffolds under both laser irradiation and nonirradiation conditions (20 min and power density: 0.85 W $cm^{-2}$). Significance levels are represented as $*p < 0.05$, $**p < 0.01$, $***p < 0.001$.

air. Within on−off cycles, the scaffold could reach a maximum temperature of 81 °C without any decrease in the temperature, suggesting the photothermal stability of the scaffolds for controlled drug release.

## NIR Light-Triggered Controlled SFN Release and Bone Cancer Cell Ablation

Cancer represents a formidable threat to human health and well-being as a malignant disease. Traditional treatment modalities such as surgery, radiotherapy, and chemotherapy come with various drawbacks, encompassing substantial tissue harm, drug resistance, cancer recurrence, and the potential for residual tumor metastasis.[64] In recent times, PTT has garnered significant attention due to its capacity to transform NIR light into localized thermal energy, enabling cancer treatment without detrimental effects on healthy cells.[65,66] In addition, the generated heat can also trigger or accelerate the release of anticancer drug locally in the tumor site enabling synergistic photothermal and chemotherapy.

To evaluate the photothermally enhanced drug release from the scaffolds, SFN[67] was chosen as a model anticancer drug. SFN serves as a protein kinase inhibitor known for its capability to hinder tumor progression. It has obtained approval for the treatment of advanced renal cell carcinoma (RCC), unresectable hepatocellular carcinoma (HCC), thyroid cancer, and challenging bone tumors.[68−71] Operating as an inhibitor for multiple tyrosine kinase receptors, SFN has the capacity to impede activation of the MAPK/ERK pathway responsible for tumor cell proliferation and metastasis. Through its binding to a range of receptors, it effectively curtails cell growth and diminishes the tumor cell population.[71] The SFN and MXene quantities in x-AF-MA-MXene-1-SFN-0 were kept the same for all of the drug release experiments to focus on the release profiles with and without laser irradiation. As substantiated by the cumulative drug release profile shown in Figure 6a,b, the SFN release from the scaffolds is significantly pH dependent. In all the experiments, a burst release of drug during the first hour of incubation has been observed, which is associated with the released drug molecules attached to the outer layer of the scaffolds by weak physical bonding such as dipole−dipole interaction to the MXene surface. The scaffolds have shown considerably high release (76%) at pH 7 and only 18% at pH 4.3 at the initial 5 h of incubation. As seen in Figure 6c, the local delivery of SFN is even amplified at pH 7 by irradiation of the scaffold at the initial incubation times.

As the tumor microenvironment is slightly acidic (pH 5.6−6.8),[72] the lower initial release at pH 4.3 is particularly interesting, considering the toxicity of antitumor drugs at higher doses. To control the drug release on demand, the photothermal effect of MXene can regulate the initial drug release in the tumor-resected implanted site. At pH 4.3, the surface zeta potential of MXene is −29 mV[73] while the surface of the SFN molecules, due to the protonation of peptide bonds, is positively charged. Thus, less cumulative release was observed without laser irradiation at acidic pH due to the stronger electrostatic interactions between MXene at the


https://doi.org/10.1021/acsmaterialsau.3c00040
ACS Mater. Au 2023, 3, 711−726

scaffold surface and protonated SFN drug. At the initial 5 h of incubation, at acidic media under laser irradiation, 35% SFN release was observed, while without laser irradiation, only 18% was observed (Figure 6d). Therefore, generated heat in the scaffold enables the on-demand release of SFN from the MXene nanosheets with controlled doses in tumor sites through performing synergistic localized hyperthermia and chemotherapy.

A temperature approximately 45 °C has been substantiated to induce the demise of tumor cells.[21] Leveraging the preceding photothermal assessment outcomes, the x-SF-MA-MXene-1 composite scaffold was harnessed for hyperthermic PTT targeting of bone tumors. The quantitative assessment of in vitro cytotoxicity and cancer cell eradication from the scaffolds was conducted by using the standard AlamarBlue assay. Osteosarcoma cells (MG-63) were cultured onto the x-SF-MA-MXene-1 scaffold, and after a 1-day incubation period, they underwent irradiation via an 808 nm laser for varying durations of 5 and 20 min, aiming to initiate photothermal ablation. As shown in Figure 6e, while in 5 min of irradiation there was no meaningful cell death due to the thermal ablation, the percentage of viable cells in 20 min laser irradiation for x-SF-MA-MXene-1 was significantly reduced.

Furthermore, as depicted in Figure 6f, akin to the control group (x-SF-MA scaffolds) without laser irradiation, the x-SF-MA-MXene-1 scaffolds exhibited 0% cell viability on the initial day of incubation, highlighting the pronounced biocompatibility of the prepared composites. In contrast, compared to the control x-SF-MA scaffolds subjected to laser irradiation, less than 32% of MG-63 cells persisted on the x-SF-MA-MXene-1 scaffolds. This finding underscores the efficacy of these scaffolds in effectively eradicating cancer cells through photothermal ablation. The same experiments were carried out for the scaffolds following 3 and 7 days of incubation, during which a higher number of viable cells were present. On the seventh day, upon subjecting the x-SF-MA-MXene-1 scaffolds to a 20 min laser irradiation, cell survival decreased to 47%, contrasting with the 227% cell viability recorded for the same group without laser irradiation. This set of photothermal investigations thus underscores the exceptional controllability and efficiency of scaffold-enabled photothermal ablation of cancer cells.

Furthermore, the occurrence of apoptosis in MG-63 cells after photothermal ablation was verified through fluorescent microscopy (cf. Figure S1). Following laser irradiation (20 min, 0.85 W $cm^{-2}$), the cells within the scaffolds, both live and dead, were stained using Calcein AM (green) and PI (red), respectively. The observation unveiled a notable distinction in fluorescence color within the x-SF-MA-MXene-1 scaffolds subjected to laser irradiation, displaying prominent red fluorescence. This outcome signifies the efficacy of cell apoptosis induced by photothermal ablation. The robustness of these findings accentuates the considerable capacity of x-SF-MA-MXene-1 scaffolds for ablating tumor cells effectively when exposed to NIR laser irradiation in an *in vitro* setting.

The aerogel swellability was evaluated by the ability of the scaffold for PBS uptake within 24 h, which were 3476% for the x-SF-MA and 2733% for the x-SF-MA-MXene-1 scaffold, respectively. This large extent of swellability ensured the possibilities for the accommodation of a large volume of media in the internal voids of scaffolds for cell seeding and cell proliferation. In the next step, preosteoblast MC3T3-E1 cells were seeded onto the scaffold surface to evaluate cell adhesion, an essential stage for demonstrating osteoconductivity and new bone tissue regeneration.[74] As evident from fluorescence images and SEM micrographs of DAPI-stained attached cells (cf. Figure 7a–f), the composite scaffolds support MC3T3-E1

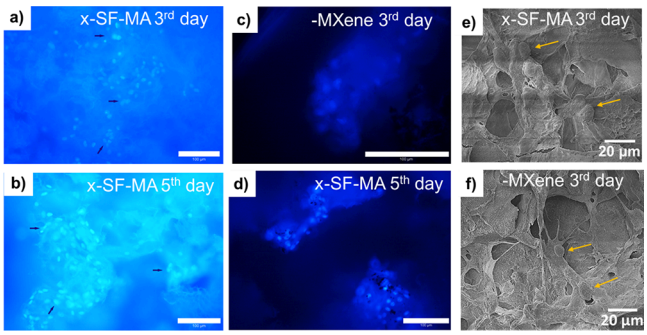


**Figure 7.** Characterization of cellular adhesion on x-SF-MA scaffolds. MC3T3-E1 cells were seeded onto x-SF-MA scaffolds, and the nuclei were stained with DAPI (blue arrows) on days 3 (a) and 5 (b). Characterization of the cellular attachment on MXene scaffolds. MC3T3-E1 cells were seeded onto MXene scaffolds and stained with DAPI (blue) at day 3 (c) and day 5 (d), scale bar: 0 $\mu$m. SEM micrographs (10×) of the attached cells on the (e) x-SF-MA and (f) x-SF-MA-MXene-1 scaffold pore surface on day 3.

cell proliferation for up to 13 days. The multiple cells were detected on the x-SF-MA on day 3, with their number enormously increasing over time (Figure 7a,b). A similar tendency was also observed for the x-SF-MA-MXene-1 scaffold. However, cell numbers dramatically increased with prolonging the incubation time compared to x-SF-MA control groups (Figure 7c,d and also see day 13 in Figure S2). In addition, no significant toxicity of the composite scaffold was observed in the MTS assay (see Figure S3). This indicates that the products released during the degradation of both the control and composite scaffolds, such as MXene ionic species, did not exhibit toxicity. This finding is consistent with prior validation by Pan et al.[18] On day 3, both the control and MXene composite aerogels exhibited a consistent structure with cellular actin filaments enveloping the scaffold surface. This coverage led to amplified cell-to-cell interactions via cytoskeleton extension and occupation of the interconnected surface within the pores on the scaffold's surface. Overall, it can be concluded that the x-SF-MA-MXene-1 is nontoxic toward osteoblast cells and can serve as an excellent extracellular matrix for its growth.

## Acellular *In Vitro* Biomineralization and Biodegradation of 3D-Printed Composite Aerogel Scaffolds

Hydroxyapatite (HAp, $Ca(PO_4)_6(OH)_2$) serves as the predominant inorganic constituent within hard tissues and is a prominent substitute for bone attributed to its biocompatibility and osteoconductivity.[75]

The capability of x-SF-MA-MXene-1 scaffolds to rapidly generate HAp crystals on their surfaces was substantiated through the observation of scaffold pore surface morphologies using SEM micrographs, as depicted in Figure 8a–g.

The SEM images demonstrate notable alterations in the micromorphology of the biomineralized scaffold matrices when compared to their plain counterparts (Figure 4f,g). Ca–P salts are formed in various amounts and sizes upon immersion in SBF. Additionally, SEM micrographs exhibit substantial shifts in the HAp morphology, progressing from small particle


https://doi.org/10.1021/acsmaterialsau.3c00040
ACS Mater. Au 2023, 3, 711–726

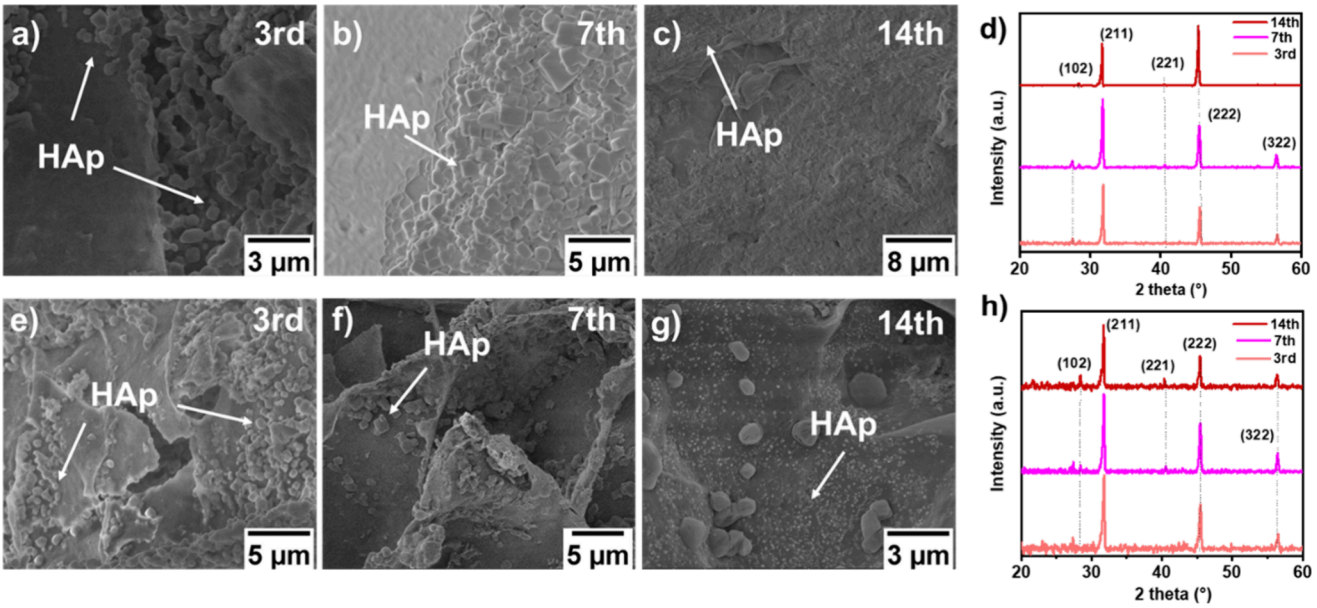


**Figure 8.** (a–c) SEM micrographs (10×) and (d) XRD pattern of x-SF-MA aerogel scaffolds upon immersion in the SBF solution for 3, 7, and 14 days. (e–g) SEM micrographs (10×) and (h) XRD pattern of x-SF-MA-MXene-1 scaffolds upon biomineralization for 3, 7, and 14 days.

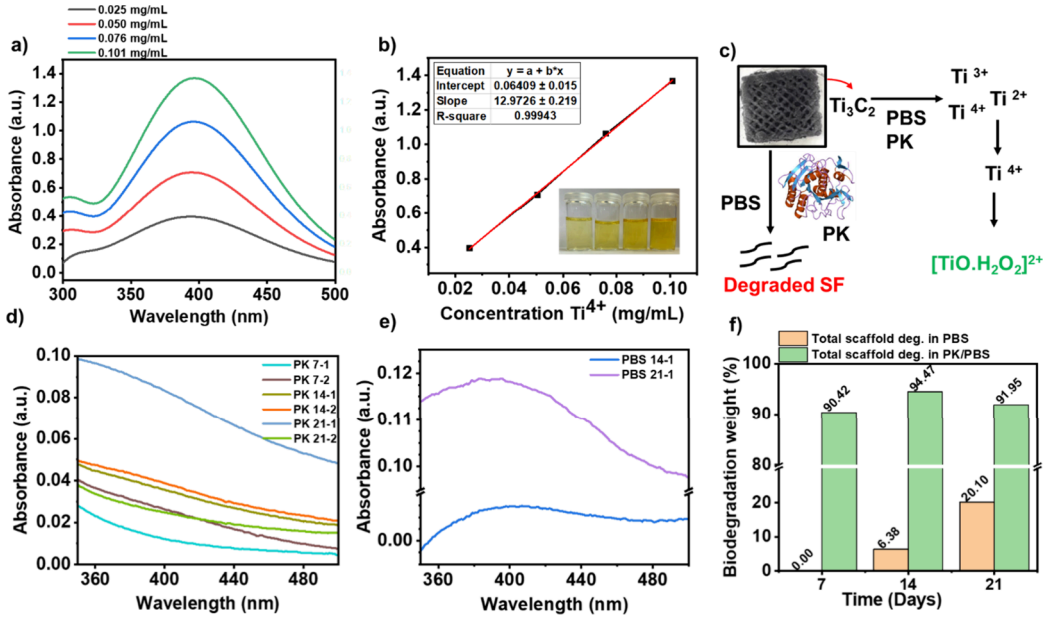


**Figure 9.** (a) UV–vis spectra of $[TiO{\cdot}H_2O_2]^{2+}$ complex ions. (b) Calibration curve for $[TiO{\cdot}H_2O_2]^{2+}$ complex concentration determination. (c) Biodegradation of x-SF-MA-MXene-1 in PK and PBS solutions; MXene degrades into the titanium ionic species, which spectrophotometric methods can measure, and SF components of scaffolds can be degraded by PK enzymatic solution using PK. (d) Absorption spectra of $[TiO{\cdot}H_2O_2]^{2+}$ in PK (0.5 U/mL) obtained from degradation solution. (e) Absorption spectra of $[TiO{\cdot}H_2O_2]^{2+}$ in PBS collected from degradation supernatant. (f) Total degradation percentage of SF-MA-30-MXene-1 aerogel-based scaffolds in 21 days.

aggregates on the third day to micrometric-sized clusters of Ca–P crystals after longer incubation periods (14th day). These changes in the HAp structure signify the surface bioactivity of both x-SF-MA and x-SF-MA-MXene-1 scaffolds, indicating their capacity to absorb the $PO_4^{3-}$ and $Ca^{2+}$ ions electrostatically.

The MXene nanosheets present on the pore surface of the composite scaffold in SBF solution at pH 7 exhibit a highly negative surface charge (−35 mV).[73] This negative charge can attract $Ca^{2+}$ ions from the SBF solution, leading to the creation of a positively charged surface layer. This layer can then adsorb $PO_4^{3-}$ ions, facilitating the nucleation and growth of apatite. The occurrence of acellular mineralization of HAp on the scaffold's surface was further validated through XRD diffractograms, as illustrated in Figure 8d,h, corresponding to incubation times of 3, 7, and 14 days in SBF. The distinctive peaks observed at around 27.4° (0, 0, 2), 31.7° (2, 1, 1), 45.3° (2, 2, 2), and 56.4° (3, 2, 2) correspond to the standard HAp crystallographic planes listed in JCPDS card number 09-0432.

For biomaterials to function efficiently, they have to be biodegradable within an acceptable period without releasing harmful metabolic products.[76] Biodegradability facilitates


https://doi.org/10.1021/acsmaterialsau.3c00040
ACS Mater. Au 2023, 3, 711–726

incremental replacement with new functional tissue. The composition and 3D structure of a scaffold can influence the biodegradation rate of a biomaterial.[76] The x-SF-MA-MXene-1 aerogel scaffold, characterized by its high porosity, facilitates easy access of enzymes to its internal structure. Through incubation of the scaffold with PBS and PK (proteolytic enzyme) solutions under gentle agitation (0 rpm, 37 °C) and continuous tracking of its weight loss at each time interval, we were able to evaluate the degradation of the SF components within the scaffold. To further investigate degradation, spectrophotometric measurements were performed, examining the formation of metal complexes between titanium ionic species and MXene in the supernatants of both PBS and PK at various time points (Figure 9a–f).

The metal–$H_2O_2$ complexes have been suggested in kinetic and computational studies for the spectrophotometric detection of titanium.[77] Under acidic conditions, the presence of titanium ions Ti(IV) together with hydrogen peroxide leads to the formation of the yellow-orange complex $[TiO{\cdot}H_2O_2]^{2+}$. This complex exhibits an absorbance at $\lambda_{max}$ = 4 nm in the UV–vis spectrum, as depicted in Figure 9a–c.The determination of this ionic complex allows the measurement of titanium species from the degradation of MXene in composite aerogel scaffolds of this study.[78] It is claimed that another species of $[Ti{\cdot}H_2O_2]^{4+}$ could also appear in the solution with higher acidity (pH < 3).[79] Still, both complex ions from Ti (IV) and $H_2O_2$ appear orange in color and have an absorption peak around 4 nm in the UV–vis spectrum.

After 14 and 21 days of incubation, 0.2 and 0.6% of MXene were degraded in PBS (cf. Figure 9e,f). Conversely, no degradation was detected in PK solutions, likely attributed to the potential interaction between the enzyme and titanium species, thereby hindering the formation of the orange complex (cf. Figure 9d,f). A significant difference is observed between the degradation rate of SF in PK (91.35% degradation in 21 days) and the degradation rate in PBS solution (19.9% degradation in 21 days) (cf. Figure 9f). Research has indicated that scaffolds made from *B. mori* experienced rapid degradation, occurring within a month, which resulted in a void that hindered the development of new tissue.[26] Combining MXene with SF appears to provide a solution by balancing the rate of scaffold degradation and the formation of new tissue *in vivo*, given that MXene exhibits a notably slow degradation rate.[80] These degradation products can follow two potential pathways: they either persist within the tissue or get metabolized by alveolar macrophages.[80]

## CONCLUSIONS

In this research, we present the creation of a novel multifunctional composite aerogel scaffold by combining self-assembled silk fibroin methacrylate (SF-MA) with $Ti_3C_2$, MXene ceramic 2D nanosheets. Through a synergistic process involving SF-MA self-assembly in solution and photo-cross-linking-assisted 3D printing, we established a hydrogel-based 3D scaffold that possesses a dual cross-linked network with multiscale porosities. Subsequently, the surface of the printed scaffold was modified with SFN-loaded MXene, leveraging its distinct physicochemical characteristics, bioactivity, and strong NIR absorption properties to confer multifunctional capabilities to the final scaffolds. The 3D-printed MXene-modified scaffolds exhibited potent photothermal conversion across various laser power densities under both wet and dry conditions. Under optimized conditions, the scaffold surface temperature could rapidly reach 47–50 °C within 2–3 min, and this temperature was maintained even after multiple cycles of laser activation and deactivation.

Furthermore, we showcased that the laser-induced heat within the scaffold not only facilitated an approximate 50% enhancement in the release of the anticancer drug (SFN) in acidic conditions but also considerably expedited drug release in both acidic and neutral pH environments. This innovation allowed for precise drug release control in response to the specific needs at the implantation site. Leveraging the heat generated by the scaffold, we harnessed its photothermal capabilities to effectively ablate and eliminate the MG-63 bone cancer cells that were cultivated on the scaffold. The outcomes of our study reveal that following a 20 min irradiation of cell-seeded composite scaffolds, the viability of the cells experienced a substantial decline (32%). Conversely, the control samples, both with and without laser irradiation, exhibited full viability. This amalgamation of photothermal-based cancer cell eradication and laser-triggered controlled anticancer drug release holds promising potential for efficiently addressing remaining bone cancer cells within resected cancer tissues.

In addition, the MXene-modified scaffolds could support the preosteoblast MC3T3-E1 cell attachment and proliferation after 5 days of incubation without any toxicity sign. Last but not least, the fabricated composite scaffold was bioactive for the mineralization of HAp crystals on the scaffold surface in 14 days of incubation with SBFs and was also biodegradable for both MXene and SF substituents.

To conclude, the developed composite aerogel scaffolds with dual functionalities hold promise as potent implants with the potential to address the challenges posed by current scaffold-based approaches in BTE post-tumor treatment. These scaffolds have the capability to serve as effective antitumoral agents while also promoting osteoconduction, offering a multifaceted solution for enhanced therapeutic outcomes.

## ASSOCIATED CONTENT

### Supporting Information

The Supporting Information is available free of charge at https://pubs.acs.org/doi/10.1021/acsmaterialsau.3c00040. Supporting Information is available from the Wiley Online Library or from the author.

Fluorescent images of live and dead MG-63 cells under laser irradiation; characterization of cellular adhesion on x-SF-MA-MXene-1 scaffolds; and evaluation of the cytocompatibility of the scaffolds (x-SF-MA and X-SF-MA-MXene-1 through indirect viability analysis of MC3T3-E1 cells (PDF)

## AUTHOR INFORMATION

### Corresponding Author

**Hajar Maleki** − *Department of Chemistry, Institute of Inorganic Chemistry, University of Cologne, Cologne 50939, Germany; Center for Molecular Medicine Cologne, CMMC Research Center, Cologne 50931, Germany*; Email: h.maleki@uni-koeln.de

### Authors

**Hadice Kübra Pektas** − *Department of Chemistry, Institute of Inorganic Chemistry, University of Cologne, Cologne 50939, Germany*



https://doi.org/10.1021/acsmaterialsau.3c00040
ACS Mater. Au 2023, 3, 711–726

**Yan. Demidov** − *Department of Chemistry, Institute of Inorganic Chemistry, University of Cologne, Cologne 50939, Germany*
**Aslin Ahvan** − *Department of Chemistry, Institute of Inorganic Chemistry, University of Cologne, Cologne 50939, Germany*
**Nahal Abie** − *Department of Chemistry, Institute of Inorganic Chemistry, University of Cologne, Cologne 50939, Germany; Department of Chemistry, Materials and Chemical Engineering, Politecnico di Milano, Milano 20054, Italy*
**Veronika S. Georgieva** − *Experimental Neonatology, Department of Pediatrics and Adolescent Medicine, University of Cologne, Cologne 50939, Germany; Center for Biochemistry, Medical Faculty, University of Cologne, Cologne 50923, Germany*
**Shiyi Chen** − *Department of Chemistry, Institute of Inorganic Chemistry, University of Cologne, Cologne 50939, Germany*
**Silvia Farè** − *Department of Chemistry, Materials and Chemical Engineering, Politecnico di Milano, Milano 20054, Italy;* orcid.org/0000-0002-0303-1131
**Bent Brachvogel** − *Experimental Neonatology, Department of Pediatrics and Adolescent Medicine, University of Cologne, Cologne 50939, Germany; Center for Biochemistry, Medical Faculty, University of Cologne, Cologne 50923, Germany*
**Sanjay Mathur** − *Department of Chemistry, Institute of Inorganic Chemistry, University of Cologne, Cologne 50939, Germany;* orcid.org/0000-0003-2765-2693

Complete contact information is available at: https://pubs.acs.org/10.1021/acsmaterialsau.3c00040

## Notes

The authors declare no competing financial interest.

## ■ ACKNOWLEDGMENTS

H.M. acknowledges the support of the German Research Foundation (Projektnummer 467116484) for financial support, the contribution of Prof. Aldo Boccaccini and Prof. Sanjay Mathur for their valuable discussion and feedback during this work, and Senol Gezgin and Dr. Thomas Remmler from the company of NETZSCH-Gerätebau GmbH Germany for their kind support in the rheological analyses of the hydrogels.

## ■ REFERENCES

(1) Speight, P. M.; Takata, T. New Tumour Entities in the 4th Edition of the World Health Organization Classification of Head and Neck Tumours: Odontogenic and Maxillofacial Bone Tumours. *Virchows Arch.* **2018**, *472* (3), 331−339.
(2) Tan, B.; Tang, Q.; Zhong, Y.; Wei, Y.; He, L.; Wu, Y.; Wu, J.; Liao, J. Biomaterial-Based Strategies for Maxillofacial Tumour Therapy and Bone Defect Regeneration. *Int. J. Oral Sci.* **2021**, *13* (1), 9.
(3) Jensdottir, T.; Buchwald, C.; Nauntofte, B.; Hansen, H. S.; Bardow, A. Saliva in Relation to Dental Erosion before and after Radiotherapy. *Acta Odontol. Scand.* **2013**, *71* (3−4), 1008−1013.
(4) Suzuki, M.; Deno, M.; Myers, M.; Asakage, T.; Takahashi, K.; Saito, K.; Mori, Y.; Saito, H.; Ichikawa, Y.; Yamamoto-Mitani, N.; Miyashita, M. Anxiety and Depression in Patients after Surgery for Head and Neck Cancer in Japan. *Palliat. Support. Care* **2016**, *14* (3), 269−277.
(5) Dewey, M. J.; Harley, B. A. C. Biomaterial Design Strategies to Address Obstacles in Craniomaxillofacial Bone Repair. *RSC Adv.* **2021**, *11* (29), 17809−17827.
(6) Bu, L.-L.; Yan, J.; Wang, Z.; Ruan, H.; Chen, Q.; Gunadhi, V.; Bell, R. B.; Gu, Z. Advances in Drug Delivery for Post-Surgical Cancer Treatment. *Biomaterials* **2019**, *219*, 119182.
(7) Li, Q.; Zhou, R.; Xie, Y.; Li, Y.; Chen, Y.; Cai, X. Sulphur-Doped Carbon Dots as a Highly Efficient Nano-Photodynamic Agent against Oral Squamous Cell Carcinoma. *Cell Prolif.* **2020**, *53* (4), No. e12786.
(8) Nasrin, A.; Hassan, M.; Gomes, V. G. Two-Photon Active Nucleus-Targeting Carbon Dots: Enhanced ROS Generation and Photodynamic Therapy for Oral Cancer. *Nanoscale* **2020**, *12* (40), 20598−20603.
(9) Mahmoodzadeh, F.; Abbasian, M.; Jaymand, M.; Salehi, R.; Bagherzadeh-Khajehmarjan, E. A Novel Gold-Based Stimuli-Responsive Theranostic Nanomedicine for Chemo-Photothermal Therapy of Solid Tumors. *Mater. Sci. Eng., C* **2018**, *93*, 880−889.
(10) Liao, J.; Jia, Y.; Chen, L.; Zhou, L.; Li, Q.; Qian, Z.; Niu, D.; Li, Y.; Li, P. Magnetic/Gold Core−Shell Hybrid Particles for Targeting and Imaging-Guided Photothermal Cancer Therapy. *J. Biomed. Nanotechnol.* **2019**, *15* (10), 2072−2089.
(11) Yang, S.; Zhou, L.; Su, Y.; Zhang, R.; Dong, C.-M. One-Pot Photoreduction to Prepare NIR-Absorbing Plasmonic Gold Nanoparticles Tethered by Amphiphilic Polypeptide Copolymer for Synergistic Photothermal-Chemotherapy. *Chin. Chem. Lett.* **2019**, *30* (1), 187−191.
(12) Lv, R.; Yang, P.; Chen, G.; Gai, S.; Xu, J.; Prasad, P. N. Dopamine-Mediated Photothermal Theranostics Combined with up-Conversion Platform under near Infrared Light. *Sci. Rep.* **2017**, *7* (1), 13562.
(13) Zhang, Z.; Zhang, J.; Tian, J.; Li, H. A Polydopamine Nanomedicine Used in Photothermal Therapy for Liver Cancer Knocks down the Anti-Cancer Target NEDD8-E3 Ligase ROC1 (RBX1). *J. Nanobiotechnol.* **2021**, *19* (1), 323.
(14) Geng, B.; Yang, D.; Pan, D.; Wang, L.; Zheng, F.; Shen, W.; Zhang, C.; Li, X. NIR-Responsive Carbon Dots for Efficient Photothermal Cancer Therapy at Low Power Densities. *Carbon* **2018**, *134*, 153−162.
(15) Boakye-Yiadom, K. O.; Kesse, S.; Opoku-Damoah, Y.; Filli, M. S.; Aquib, M.; Joelle, M. M. B.; Farooq, M. A.; Mavlyanova, R.; Raza, F.; Bavi, R.; Wang, B. Carbon Dots: Applications in Bioimaging and Theranostics. *Int. J. Pharm.* **2019**, *564*, 308−317.
(16) Yan, M.; Liu, Y.; Zhu, X.; Wang, X.; Liu, L.; Sun, H.; Wang, C.; Kong, D.; Ma, G. Nanoscale Reduced Graphene Oxide-Mediated Photothermal Therapy Together with IDO Inhibition and PD-L1 Blockade Synergistically Promote Antitumor Immunity. *ACS Appl. Mater. Interfaces* **2019**, *11* (2), 1876−1885.
(17) Cao, J.; An, H.; Huang, X.; Fu, G.; Zhuang, R.; Zhu, L.; Xie, J.; Zhang, F. Monitoring of the Tumor Response to Nano-Graphene Oxide-Mediated Photothermal/Photodynamic Therapy by Diffusion-Weighted and BOLD MRI. *Nanoscale* **2016**, *8* (19), 10152−10159.
(18) Pan, S.; Yin, J.; Yu, L.; Zhang, C.; Zhu, Y.; Gao, Y.; Chen, Y. 2D MXene-Integrated 3D-Printing Scaffolds for Augmented Osteosarcoma Phototherapy and Accelerated Tissue Reconstruction. *Adv. Sci.* **2020**, *7* (2), 1901511.
(19) Lee, S. H.; Kang, M. S.; Jeon, S.; Jo, H. J.; Hong, S. W.; Kim, B.; Han, D.-W. 3D Bioprinting of Human Mesenchymal Stem Cells-Laden Hydrogels Incorporating MXene for Spontaneous Osteodifferentiation. *Heliyon* **2023**, *9* (3), No. e14490.
(20) Wang, X.; Xue, J.; Ma, B.; Wu, J.; Chang, J.; Gelinsky, M.; Wu, C. Black Bioceramics: Combining Regeneration with Therapy. *Adv. Mater.* **2020**, *32* (48), 2005140.
(21) Liao, J.; Han, R.; Wu, Y.; Qian, Z. Review of a New Bone Tumor Therapy Strategy Based on Bifunctional Biomaterials. *Bone Res.* **2021**, *9* (1), 18.
(22) Ma, H.; Li, T.; Huan, Z.; Zhang, M.; Yang, Z.; Wang, J.; Chang, J.; Wu, C. 3D Printing of High-Strength Bioscaffolds for the Synergistic Treatment of Bone Cancer. *NPG Asia Mater.* **2018**, *10* (4), 31−44.
(23) Dong, S.; Chen, Y.; Yu, L.; Lin, K.; Wang, X. Magnetic Hyperthermia−Synergistic H2O2 Self-Sufficient Catalytic Suppression of Osteosarcoma with Enhanced Bone-Regeneration Bioactivity

by 3D-Printing Composite Scaffolds. *Adv. Funct. Mater.* **2020**, *30* (4), 1907071.
(24) Yang, F.; Lu, J.; Ke, Q.; Peng, X.; Guo, Y.; Xie, X. Magnetic Mesoporous Calcium Sillicate/Chitosan Porous Scaffolds for Enhanced Bone Regeneration and Photothermal-Chemotherapy of Osteosarcoma. *Sci. Rep.* **2018**, *8* (1), 7345.
(25) Li, D.; Nie, W.; Chen, L.; McCoul, D.; Liu, D.; Zhang, X.; Ji, Y.; Yu, B.; He, C. Self-Assembled Hydroxyapatite-Graphene Scaffold for Photothermal Cancer Therapy and Bone Regeneration. *J. Biomed. Nanotechnol.* **2018**, *14*, 2003−2017.
(26) Maleki, H.; Shahbazi, M.-A.; Montes, S.; Hosseini, S. H.; Eskandari, M. R.; Zaunschirm, S.; Verwanger, T.; Mathur, S.; Milow, B.; Krammer, B.; Hüsing, N. Mechanically Strong Silica-Silk fibroin Bioaerogel: A Hybrid Scaffold with Ordered Honeycomb Micromorphology and multiscale Porosity for Bone Regeneration. *ACS Appl. Mater. Interfaces* **2019**, *11* (19), 17256−17269.
(27) Maleki, H.; Durães, L.; García-González, C. A.; del Gaudio, P.; Portugal, A.; Mahmoudi, M. Synthesis and Biomedical Applications of aerogels: Possibilities and Challenges. *Adv. Colloid Interface Sci.* **2016**, *236*, 1−27.
(28) Karamat-Ullah, N.; Demidov, Y.; Schramm, M.; Grumme, D.; Auer, J.; Bohr, C.; Brachvogel, B.; Maleki, H. 3D Printing of Antibacterial, Biocompatible, and Biomimetic Hybrid Aerogel-Based Scaffolds with Hierarchical Porosities via Integrating Antibacterial Peptide-Modified Silk fibroin with Silica Nanostructure. *ACS Biomater. Sci. Eng.* **2021**, *7* (9), 4545−4556.
(29) Qi, Y.; Wang, H.; Wei, K.; Yang, Y.; Zheng, R.-Y.; Kim, I. S.; Zhang, K.-Q. A Review of Structure Construction of Silk fibroin Biomaterials from Single Structures to Multi-Level Structures. *Int. J. Mol. Sci.* 2017, *18* (3) 237. .
(30) Al-Jawuschi, N.; Chen, S.; Abie, N.; Fischer, T.; Fare, S.; Maleki, H. H. Self-Assembly-Driven $Bi_2S_3$ Nanobelts Integrated a Silk-fibroin-Based 3D-Printed Aerogel-Based Scaffold with a Dual-Network Structure for Photothermal Bone Cancer Therapy. *Langmuir* **2023**, *39* (12), 4326−4337.
(31) Rockwood, D. N.; Preda, R. C.; Yücel, T.; Wang, X.; Lovett, M. L.; Kaplan, D. L. Materials Fabrication from Bombyx Mori Silk fibroin. *Nat. Protoc.* **2011**, *6* (10), 1612−1631.
(32) Sofia, S.; McCarthy, M. B.; Gronowicz, G.; Kaplan, D. L. Functionalized Silk-Based Biomaterials for Bone Formation. *J. Biomed. Mater. Res.* **2001**, *54* (1), 139−148.
(33) Janani, G.; Kumar, M.; Chouhan, D.; Moses, J. C.; Gangrade, A.; Bhattacharjee, S.; Mandal, B. B. Insight into Silk-Based Biomaterials: From Physicochemical Attributes to Recent Biomedical Applications. *ACS Appl. Bio Mater.* **2019**, *2* (12), 5460−5491.
(34) Nguyen, T. P.; Nguyen, Q. V.; Nguyen, V.-H.; Le, T.-H.; Huynh, V. Q.; Vo, D.-V. N.; Trinh, Q. T.; Kim, S. Y.; Le, Q. V. Silk fibroin-Based Biomaterials for Biomedical Applications: A Review. *Polymers* **2019**, *11* (12)1933. .
(35) Wang, Y.; Kim, B. J.; Peng, B.; Li, W.; Wang, Y.; Li, M.; Omenetto, F. G. Controlling Silk fibroin Conformation for Dynamic, Responsive, Multifunctional Micropatterned Surfaces. *Proc. Natl. Acad. Sci.* **2019**, *116* (43), 21361−21368.
(36) Maleki, H.; Montes, S.; Hayati-Roodbari, N.; Putz, F.; Huesing, N. Compressible, Thermally Insulating, and Fire Retardant aerogels through Self-Assembling Silk fibroin Biopolymers Inside a Silica Structure—An Approach towards 3D Printing of aerogels. *ACS Appl. Mater. Interfaces* **2018**, *10* (26), 22718−22730.
(37) Maleki, H.; Whitmore, L.; Hüsing, N. Novel Multifunctional Polymethylsilsesquioxane−Silk fibroin Aerogel Hybrids for Environmental and Thermal Insulation Applications. *J. Mater. Chem. A* **2018**, *6* (26), 12598−12612.
(38) Ng, P.; Pinho, A. R.; Gomes, M. C.; Demidov, Y.; Krakor, E.; Grume, D.; Herb, M.; Lê, K.; Mano, J.; Mathur, S.; Maleki, H. Fabrication of Antibacterial, Osteo-Inductor 3D Printed Aerogel-Based Scaffolds by Incorporation of Drug Laden Hollow Mesoporous Silica Microparticles into the Self-Assembled Silk fibroin Biopolymer. *Macromol. Biosci.* **2022**, *22* (4), 2100442.
(39) Bruder, V.; Ludwig, T.; Opitz, S.; Christoffels, R.; Fischer, T.; Maleki, H. Hierarchical Assembly of Surface Modified Silk fibroin Biomass into Micro-, and Milli-Metric Hybrid aerogels with Core-Shell, Janus, and Composite Configurations for Rapid Removal of Water Pollutants. *Adv. Mater. Interfaces* **2021**, *8* (5), No. 2001892. In press
(40) Bandar Abadi, M.; Weissing, R.; Wilhelm, M.; Demidov, Y.; Auer, J.; Ghazanfari, S.; Anasori, B.; Mathur, S.; Maleki, H. Nacre-Mimetic, Mechanically Flexible, and Electrically Conductive Silk fibroin-MXene Composite Foams as Piezoresistive Pressure Sensors. *ACS Appl. Mater. Interfaces* **2021**, *13* (29), 34996−35007.
(41) Zheng, Z.; Guo, S.; Liu, Y.; Wu, J.; Li, G.; Liu, M.; Wang, X.; Kaplan, D. Lithium-Free Processing of Silk fibroin. *J. Biomater. Appl.* **2016**, *31* (3), 450−463.
(42) Lim, K. R. G.; Shekhirev, M.; Wyatt, B. C.; Anasori, B.; Gogotsi, Y.; Seh, Z. W. Fundamentals of MXene Synthesis. *Nat. Synth.* **2022**, *1* (8), 601−614.
(43) Kokubo, T.; Takadama, H. Simulated Body Fluid (SBF) as a Standard Tool to Test the Bioactivity of Implants. *Handb. Biominer.* **2007**, 97−109.
(44) Chen, M. H.; Wang, L. L.; Chung, J. J.; Kim, Y.-H.; Atluri, P.; Burdick, J. A. Methods To Assess Shear-Thinning Hydrogels for Application As Injectable Biomaterials. *ACS Biomater. Sci. Eng.* **2017**, *3* (12), 3146−3160.
(45) Shao, G.; Hanaor, D. A. H.; Shen, X.; Gurlo, A. Freeze Casting: From Low-Dimensional Building Blocks to Aligned Porous Structures—A Review of Novel Materials, Methods, and Applications. *Adv. Mater.* **2020**, *32* (17), 1907176.
(46) Shahbazi, M.-A.; Ghalkhani, M.; Maleki, H. Directional Freeze-Casting: A Bioinspired Method to Assemble Multifunctional Aligned Porous Structures for Advanced Applications. *Adv. Eng. Mater.* **2020**, *22* (7), 2000033.
(47) Bai, H.; Chen, Y.; Delattre, B.; Tomsia, A. P.; Bidirectional Freeze Casting for Fabricating Lamellar Structures. US20170100857A1.
(48) Alhabeb, M.; Maleski, K.; Anasori, B.; Lelyukh, P.; Clark, L.; Sin, S.; Gogotsi, Y. Guidelines for Synthesis and Processing of Two-Dimensional Titanium Carbide (Ti3C2Tx MXene). *Chem. Mater.* **2017**, *29* (18), 7633−7644.
(49) Gogotsi, Y.; Anasori, B. The Rise of MXenes. *ACS Nano* **2019**, *13* (8), 8491−8494.
(50) VahidMohammadi, A.; Rosen, J.; Gogotsi, Y. The World of Two-Dimensional Carbides and Nitrides (MXenes). *Science* **2021**, *372* (6547), No. eabf1581.
(51) Chen, L.; Dai, X.; Feng, W.; Chen, Y. Biomedical Applications of MXenes: From Nanomedicine to Biomaterials. *Acc. Mater. Res.* **2022**, *3* (8), 785−798.
(52) Huang, J.; Li, Z.; Mao, Y.; Li, Z. Progress and Biomedical Applications of MXenes. *Nano Sel.* **2021**, *2* (8), 1480−1508.
(53) Zamhuri, A.; Lim, G. P.; Ma, N. L.; Tee, K. S.; Soon, C. F. MXene in the Lens of Biomedical Engineering: Synthesis, Applications and Future Outlook. *Biomed. Eng. OnLine* **2021**, *20* (1), 33.
(54) Huang, Z.; Cui, X.; Li, S.; Wei, J.; Li, P.; Wang, Y.; Lee, C.-S. Two-Dimensional MXene-Based Materials for Photothermal. *Therapy.* **2020**, *9* (8), 2233−2249.
(55) Perini, G.; Rosenkranz, A.; Friggeri, G.; Zambrano, D.; Rosa, E.; Augello, A.; Palmieri, V.; De Spirito, M.; Papi, M. Advanced Usage of Ti3C2Tx MXenes for Photothermal Therapy on Different 3D Breast Cancer Models. *Biomed. Pharmacother.* **2022**, *153*, 113496.
(56) Lin, H.; Gao, S.; Dai, C.; Chen, Y.; Shi, J. A Two-Dimensional Biodegradable Niobium Carbide (MXene) for Photothermal Tumor Eradication in NIR-I and NIR-II biowindows. *J. Am. Chem. Soc.* **2017**, *139* (45), 16235−16247.
(57) Zainuddin; Le, T. T.; Park, Y.; Chirila, T. V.; Halley, P. J.; Whittaker, A. K. The Behavior of Aged Regenerated Bombyx Mori Silk fibroin Solutions Studied by 1H NMR and Rheology. *Biomaterials* **2008**, *29* (32), 4268−4274.


https://doi.org/10.1021/acsmaterialsau.3c00040
*ACS Mater. Au* 2023, 3, 711−726

(58) Ohgo, K.; Bagusat, F.; Asakura, T.; Scheler, U. Investigation of Structural Transition of Regenerated Silk fibroin Aqueous Solution by Rheo-NMR Spectroscopy. *J. Am. Chem. Soc.* **2008**, *130* (12), 4182−4186.
(59) Asakura, T. Structure of Silk I (Bombyx Mori Silk fibroin before Spinning) -Type II β-Turn, Not α-Helix-. *Molecules* 2021, *26* (12) 3706. .
(60) Qian, A.; Seo, J. Y.; Shi, H.; Lee, J. Y.; Chung, C.-H. Surface Functional Groups and Electrochemical Behavior in Dimethyl Sulfoxide-Delaminated Ti3C2Tx MXene. *Chemsuschem* **2018**, *11* (21), 3719−3723.
(61) Li, M.; Ogiso, M.; Minoura, N. Enzymatic Degradation Behavior of Porous Silk fibroin Sheets. *Biomaterials* **2003**, *24* (2), 357−365.
(62) Lee, D. J.; Kwon, J.; Kim, Y.-I.; Wang, X.; Wu, T.-J.; Lee, Y.-T.; Kim, S.; Miguez, P.; Ko, C.-C. Effect of Pore Size in Bone Regeneration Using Polydopamine-Laced Hydroxyapatite Collagen Calcium Silicate Scaffolds Fabricated by 3D Mould Printing Technology. *Orthod. Craniofac. Res.* **2019**, *22* (S1), 127−133.
(63) Kumar, A. V. P.; Dubey, S. K.; Tiwari, S.; Puri, A.; Hejmady, S.; Gorain, B.; Kesharwani, P. Recent Advances in Nanoparticles Mediated Photothermal Therapy Induced Tumor Regression. *Int. J. Pharm.* **2021**, *606*, 120848.
(64) Bosma, S. E.; Wong, K. C.; Paul, L.; Gerbers, J. G.; Jutte, P. C. A Cadaveric Comparative Study on the Surgical Accuracy of Freehand, Computer Navigation, and Patient-Specific Instruments in Joint-Preserving Bone Tumor Resections. *Sarcoma* **2018**, *2018*, 4065846.
(65) Chu, K. F.; Dupuy, D. E. Thermal Ablation of Tumours: Biological Mechanisms and Advances in Therapy. *Nat. Rev. Cancer* **2014**, *14* (3), 199−208.
(66) Liu, Y.; Bhattarai, P.; Dai, Z.; Chen, X. Photothermal Therapy and Photoacoustic Imaging via Nanotheranostics in Fighting Cancer. *Chem. Soc. Rev.* **2019**, *48* (7), 2053−2108.
(67) Kong, F.-H.; Ye, Q.-F.; Miao, X.-Y.; Liu, X.; Huang, S.-Q.; Xiong, L.; Wen, Y.; Zhang, Z.-J. Current Status of Sorafenib Nanoparticle Delivery Systems in the Treatment of Hepatocellular Carcinoma. *Theranostics* **2021**, *11* (11), 5464−5490.
(68) Li, Y.; Gao, Z.-H.; Qu, X.-J. The Adverse Effects of Sorafenib in Patients with Advanced Cancers. *Basic Clin. Pharmacol. Toxicol.* **2015**, *116* (3), 216−221.
(69) Strumberg, D.; Clark, J. W.; Awada, A.; Moore, M. J.; Richly, H.; Hendlisz, A.; Hirte, H. W.; Eder, J. P.; Lenz, H.-J.; Schwartz, B. Safety, Pharmacokinetics, and Preliminary Antitumor Activity of Sorafenib: A Review of Four Phase I Trials in Patients with Advanced Refractory Solid Tumors. *Oncologist* **2007**, *12* (4), 426−437.
(70) Raciborska, A.; Bilska, K. Sorafenib in Patients with Progressed and Refractory Bone Tumors. *Med. Oncol.* **2018**, *35* (10), 126.
(71) Coventon, J. A Review of the Mechanism of Action and Clinical Applications of Sorafenib in Advanced Osteosarcoma. *J. Bone Oncol.* **2017**, *8*, 4−7.
(72) Boedtkjer, E.; Pedersen, S. F. The Acidic Tumor Microenvironment as a Driver of Cancer. *Annu. Rev. Physiol.* **2020**, *82* (1), 103−126.
(73) Li, Y.; Zhou, X.; Wang, J.; Deng, Q.; Li, M.; Du, S.; Han, Y.-H.; Lee, J.; Huang, Q. Facile Preparation of in Situ Coated Ti3C2Tx/Ni0.5Zn0.5Fe2O4 Composites and Their Electromagnetic Performance. *RSC Adv.* **2017**, *7* (40), 24698−24708.
(74) Vaccaro, Alexander R. The Role of the Osteoconductive Scaffold in Synthetic Bone Graft. *Orthopedics* **2002**, *25* (5), S571−S578.
(75) Wu, X.; Walsh, K.; Hoff, B. L.; Camci-Unal, G. Mineralization of Biomaterials for Bone Tissue Engineering. *Bioengineering* **2020**, *7* (4) 132. 10.339r0/bioengineering7040132.
(76) Gerhardt, L.-C.; Boccaccini, A. R. Bioactive Glass and Glass-Ceramic Scaffolds for Bone Tissue Engineering. *Materials* **2010**, *3* (7), 3867−3910.
(77) Wallen, C. M.; Bacsa, J.; Scarborough, C. C. Coordination of Hydrogen Peroxide with Late-Transition-Metal Sulfonamido Complexes. *Inorg. Chem.* **2018**, *57* (9), 4841−4848.
(78) Peruzzo, V.; Hester, R. E. A Study of the Ti(III)-H2O2-SCN− Reaction. *Inorg. Chim. Acta* **1976**, *20*, 145−148.
(79) Wallen, C. M.; Bacsa, J.; Scarborough, C. C. Hydrogen Peroxide Complex of Zinc. *J. Am. Chem. Soc.* **2015**, *137* (46), 14606−14609.
(80) Naskar, D.; Ghosh, A. K.; Mandal, M.; Das, P.; Nandi, S. K.; Kundu, S. C. Dual Growth Factor Loaded Nonmulberry Silk fibroin/Carbon Nanofiber Composite 3D Scaffolds for in Vitro and in Vivo Bone Regeneration. *Biomaterials* **2017**, *136*, 67−85.


https://doi.org/10.1021/acsmaterialsau.3c00040
*ACS Mater. Au* 2023, 3, 711−726